Corrosion performance of slurry aluminide coatings in molten NaCl–KCl

B. Grégoire, C. Oskay, T.M. Meißner, M.C. Galetz

https://doi.org/10.1016/j.solmat.2021.110974

Corrosion performance of slurry aluminide coatings in molten NaCl-KCl

B. Grégoire*, C. Oskay, T.M. Meißner, M.C. Galetz*

DECHEMA-Forschungsinstitut, Theodor-Heuss-Allee 25, 60486 Frankfurt am Main, Germany

* Corresponding authors: benjamin.gregoire@dechema.de (B. Grégoire), mathias.galetz@dechema.de (M.C. Galetz)

ABSTRACT

The corrosion performance of water-based slurry aluminide coatings elaborated on iron- and nickel-based materials is investigated in molten chlorides as candidate heat transfer fluids (HTF) for thermal energy storage (TES) in third generation concentrated solar power (CSP) plants. This work presents a screening of four different materials (ferritic-martensitic P91 steel, austenitic stainless steel 316L, Inconel 600 and high-purity nickel) to investigate the influence of the alloying elements (e.g. Fe, Cr, Ni contents) on the microstructure and corrosion performance of slurry aluminide coatings. Individual metallic samples were diffusion-coated with slurries containing Al microparticles and subsequently exposed to molten NaCl-KCl at 700°C for 100 h under argon. The experimental observations indicate that the performance of the aluminide coatings is governed by the precipitation of secondary phases within the B2 aluminide matrix rather than its intrinsic Al concentration (where B2 refers to either FeAl, (Fe,Ni)Al or NiAl intermetallic compounds). Of those, Fe-rich aluminide coatings were found to be more resistant to molten chlorides than Ni-rich ones. This is attributed to the greater solubility of Cr in iron aluminides than in nickel aluminides, preventing the precipitation of Cr-rich intermetallic compounds and/or Cr-rich carbides within the B2 matrix. Cr-rich phases were selectively dissolved upon exposure leaving the coating matrix with void channels. According to residual coating thickness measurements, the following ranking with increasing corrosion resistance can be given for Al-slurry coated materials: Inconel 600 < high-purity nickel < austenitic stainless steel 316L < ferritic-martensitic P91 steel.

Keywords: Concentrated solar power (CSP); Molten chlorides; Corrosion; Aluminide coatings; Al-slurry; Iron- and nickel-based materials

1. Introduction

With the ultimate goal of reducing greenhouse gases emissions, concentrated solar power (CSP) is one of the most promising technologies to harvest clean electricity from a renewable and abundant source of energy. The most common concentrator configurations include parabolic troughs, solar power towers, parabolic dishes and linear Fresnel reflectors [1,2]. Whereas parabolic trough is a still highly installed configuration, accounting for more than 90% of the total CSP installed capacity, recent trends show that solar power tower system is increasingly competitive owing to its capability to achieve higher temperatures for increased thermodynamic efficiency [3]. In addition, the large thermal energy storage (TES) capacity of solar power tower systems considerably improves the cost-competitiveness of the CSP technology by extending the time during which the plant can generate power without solar radiation [4,5].

In a solar power tower system, a field of programmable mirrors (*heliostats*) concentrates the solar radiation onto a central absorber where the focused energy heats up the receiver tubes and the heat transfer fluid (HTF) directed through them. The heated fluid, currently composed of molten nitrate salts in commercial CSP plants [2,5,6], is then transferred to a heat exchanger to produce steam [1]. The steam then flows through a conventional turbine attached to a generator to produce electricity. Alternatively, the excess heated fluid is stored in a large vessel (i.e. hot storage tank) for later use to maintain a constant power generation after sunset. After flowing through the thermal exchanger, the cooled fluid is then stored in a cold storage tank above its freezing point where

it can be pumped on demand up to the top of the solar receiver to be heated again. Despite the considerable advantages of using molten salts as HTF and TES materials, including high thermal conductivity, high heat capacity and relatively low viscosity, they are also highly corrosive when in contact with metallic structural components [1,4,7,8]. In addition, the use of molten chloride salts is envisaged for the third generation of CSP with the objective to operate at higher temperatures than the state-of-the-art *Solar Salt* of molten nitrates and to power a supercritical carbon dioxide (s-CO_2) Brayton cycle for improved efficiency and reduced costs of power generation [7,9,10]. Using molten chloride salts as HTF and for TES at elevated temperatures makes it even more challenging to maintain tolerable corrosion rates for structural materials (around 20 µm/year) [9,11]. The understanding of the corrosion mechanisms and the use of appropriate mitigation strategies are therefore essential to ensure constant power generation over the 30 years expected lifetime of CSP plants.

Depending on the operating temperature and the required mechanical strength, various low-alloyed steels, stainless steels and nickel-based alloys are employed for piping and containment materials in contact with molten salts in CSP plants. This led to intensive research to investigate the corrosion behavior of such alloys and their weld joints in molten salts. In the particular case of molten chlorides, numerous recent studies reported on the corrosiveness of different binary and ternary chloride mixtures towards metallic substrates [11-22]. Even though some measures can significantly reduce the corrosion kinetics including the use of inert atmospheres or purifying the salts before exposure, local variation in the operating conditions may lead to very high corrosion rates in molten chlorides [21,22] and potentially to leakage issues in storage tanks and piping systems. Furthermore, most of the corrosion studies at laboratory scale focused on the surface reactivity of alloys with molten chlorides, yet their combination with external mechanical loads and erosion effects due to dynamic salt flow would further shorten the lifetime of metallic structures (e.g. stress-corrosion cracking and related mechanisms). This focuses the motivation on adequately performing the purification of the salt and controlling the level of impurities (e.g. oxygen, water) in the ullage gas throughout the life of the CSP plant.

The electrochemical nature of the corrosion attack of metals and alloys by molten chlorides has long been acknowledged [23,24]. Regardless of the chloride compounds present in the melt, the corrosion of iron- and nickel-based alloys is always associated with the selective dissolution of Cr [15-18,21]. This is in good agreement with the electromotive force series of metals in molten chlorides with, in the order of increasing standard potential, $Al^{3+}/Al < Mn^{2+}/Mn < Cr^{2+}/Cr < Fe^{2+}/Fe < Ni^{2+}/Ni$ [25,26] as well as the lack to form a scale (Cr dissolution). As one of the main alloying elements in steels and nickel-based alloys and being more active than Fe and Ni, Cr is indeed expected to be dissolved preferentially. However, until recently, no investigation focused on determining whether Cr was directly dissolved from the metallic matrix or as a result of the precipitation of secondary Cr-rich phases within the alloys. Experimental observations of Abramov et al. [19,20] and by our group [21,22] highlighted the influence of secondary Cr-rich phases and their further dissolution on the corrosion mechanisms of iron- and nickel-based alloys in molten chlorides. The corrosion mechanisms proposed in Refs. [21,22] involve the formation of micro-galvanic pairs between the secondary Cr-rich phases (anodic sites) and the alloy metallic matrix (cathode) in contact with the electrolyte. The larger the cathode to anode volume ratio is, the faster the dissolution of these Cr-rich phases. The subsequent Cr diffusion flux from the substrate therefore results in the formation of a porous metallic matrix depleted in Cr. Since the oxygen partial pressure is very low at the salt/metal interface, the formation of volatile metal chloride compounds such as $CrCl_2$ occurs further accelerating the corrosion kinetics. Nickel-based alloys are usually more corrosion resistant than steels in molten chlorides with high Mo-containing nickel-based alloys (e.g. Hastelloy C-276) being the best candidates for piping/container material [1,15]. Nevertheless, such alloys are quite expensive and still show corrosion rates far from industrial requirements, which shows the need for corrosion mitigation strategies in molten chlorides.

Among the different mitigation strategies that can be developed to improve the corrosion behavior of structural materials in molten salts, the use of alumina-former coatings is promising [13,14,18]. In this context, slurry aluminide coatings were found to be particularly beneficial in protecting metallic substrates from corrosion in molten nitrates [27,28,29] and in molten carbonates [30]. The protective behavior of slurry aluminide coatings in these salts is ensured by the formation of a thin and protective alumina scale on the surfaces. If the oxide scale gets

damaged in the form of cracks or by spallation, Al is supplied by the large Al reservoir for re-healing of the Al_2O_3 scale. It is worth mentioning that slurry diffusion coating is a cost-effective technique to coat large components such as pipes, vessels and also permits on-site and local repair of damaged components [31], which offers great versatility for CSP applications. However, the corrosion performance of slurry aluminide coatings in molten chlorides at low oxygen partial pressure has not been studied in the literature and only very few studies investigated the corrosion behavior of bulk intermetallic compounds of FeAl and NiAl in molten chlorides under combustion conditions [32,33]. The present work therefore proposes to bridge this gap.

Four different iron- and nickel-based materials (ferritic-martensitic P91 steel, stainless steel 316L, Inconel 600 and high-purity nickel) were diffusion coated with Al microparticles containing water-based slurry solutions. To investigate the corrosion performance of the slurry aluminide coatings, coated samples were exposed in molten NaCl-KCl at 700°C for 100 h in Ar. The NaCl-KCl eutectic mixture (44.5-55.5 in wt.%, respectively) was selected as it forms the basis of many ternary chloride mixture candidates for CSP applications [9,34]. The results obtained for coated materials were compared with the corrosion mechanisms of uncoated ferritic-martensitic P91 steel and Inconel 600 elucidated in Ref. [21] in similar testing conditions. In this study, the degradation and protection mechanisms of the slurry aluminide coatings are presented in light of the microstructural characterization of as-coated and exposed Al-slurry coated materials.

2. Experimental procedures

2.1. Materials

The chemical compositions of the investigated materials are compiled in Table 1. For a better understanding of the corrosion behavior of slurry aluminide coatings in molten chlorides, three industrial alloys (ferritic-martensitic P91 steel, stainless steel 316L and Inconel 600) as well as high-purity nickel were selected in this study. This selection was expected to provide a screening range between Fe-rich to Ni-rich aluminide intermetallics and highlight the influence of additional alloying elements (e.g. Cr, Mn) on the corrosion behavior of Al-slurry coated alloys. In addition to their current uses in a wide range of structural applications, it should be noted that ferritic-martensitic P91 steel, stainless steel 316L and Inconel 600 are all TES containment material candidates for CSP applications [7]. The study of their chemical compatibility and of the ways to mitigate corrosion in molten salts is therefore critical to ensure the development and durability of next-generation CSP plants.

Table 1
Nominal chemical compositions in wt.% of the materials investigated in this study.

Substrate	Fe	Cr	Ni	Mo	Mn	Si	C	N	Others
P91 (1.4903)	Bal.	8.0-9.5	≤ 0.40	0.85-1.05	0.30-0.60	0.20-0.50	0.08-0.12	0.03-0.07	V: 0.18-0.25 Nb: 0.06-0.10
316L (1.4404)	Bal.	16.5-18.5	10.0-13.0	2.0-2.5	≤ 2.00	≤ 1.00	≤ 0.03	≤ 0.10	-
Inconel 600 (2.4816)	6.0-10.0	14.0-17.0	Bal.	-	≤ 1.00	≤ 0.50	≤ 0.15	-	Cu: ≤ 0.50 Ti: ≤ 0.30
Ni	15 ppm	≤ 1 ppm	99.99	-	≤ 1 ppm	2 ppm	-	-	Cu: 3 ppm

2.2. Sample preparation and coating manufacturing

As-received Inconel 600 (VDM Metals) plates were machined into rectangular samples of 25 mm x 5 mm x 3 mm dimensions, respectively 25 mm x 6 mm x 3mm for as-received ferritic-martensitic P91 steel (Vallourec), stainless steel 316L (ThyssenKrupp) and high-purity nickel (GoodFellow) plates. A small hole (1.5 mm diameter) was drilled on each sample to allow for a more convenient positioning of the samples in the slurry coating furnace and for the corrosion experiments. The metallic samples were then ground with P180 SiC paper, washed with

distilled water and ultrasonically cleaned in ethanol before slurry deposition. The slurry formulation was composed of 1.3 parts by weight PolyVinyl Alcohol (PVA)/deionized water solution, hereafter named as the organic binder, to 1 part by weight spherical Al particles (mean diameter of 10 µm). After mixing, the Al-containing slurries were deposited by air brush on all surfaces of the samples at room temperature. Two successive layers were deposited on all surfaces to ensure a good coverage by the slurries while a drying step of 30 minutes was observed between each layer. The samples were periodically weighed with a 10^{-5} g precision balance to control the deposited slurry quantity (≈10 $mg.cm^{-2}$ corresponding to a dry slurry thickness of approximately 50 µm).

After deposition of the Al-containing slurry, the samples were introduced in a horizontal quartz tube furnace to conduct the diffusion heat treatment. The sealed reaction chamber was then evacuated with a vacuum pump and purged with argon three successive times to limit the residual oxygen partial pressure. Before heating, the furnace was filled a last time with argon and was ventilated with a flow of argon throughout the run to prevent any significant oxidation of the Al microparticles and of the metallic substrates. The heat treatment parameters for iron-based and nickel-based materials are summarized in Table 2. In both cases, the heating ramps were fixed at 5°C/min and a systematic step at 400°C for 3 h was observed to decompose the organic binder. The aluminizing step was then performed at 650°C for 3 h to form intermetallic coatings following self-propagating high-temperature synthesis reactions [35]. Since the aluminizing treatment was performed at low temperature (650°C) and pure Al microparticles were used as donors, this coating process is considered as a high-activity process which usually leads to the formation of brittle Al-rich intermetallic phases such as Fe_2Al_5 [36,37] and Ni_2Al_3 [31,38]. In order to stabilize the B2-ordered structures (i.e. FeAl, (Fe,Ni)Al or NiAl depending on the substrates composition), an additional annealing step at high temperature was performed. For the iron-based materials, the 1050°C-0.5 h annealing step was selected as the conventional normalizing treatment of P91 grade steel [39] and recommended annealing treatment of stainless steel 316L [40]. For Inconel 600 and high-purity nickel, a 1100°C-2 h annealing step was considered following the recommended solution annealing of Inconel 600 [41]. After the annealing step, the samples were left in the reaction chamber for cooling and removed when the furnace was sufficiently cooled (< 50°C). After coating manufacturing, the samples were ultrasonically cleaned in ethanol in order to remove the slurry residues (i.e. alumina shells [35,38]). It is worth noting that a tempering treatment of ferritic-martensitic P91 steel was not conducted in this study since the objective was to focus on the corrosion performance of the aluminide coatings and that quenching could not be performed due to the thermal inertia of the furnace. For industrial applications, a tempering treatment (e.g. 780°C-2 h followed by quenching) could be included in the coating process to recover the initial microstructure of the alloy and its mechanical properties.

Table 2
Summary of the heat treatment parameters for Al-slurry diffusion coatings.

Substrate	Heating ramps	Binder removal	Aluminizing step	Annealing step	Atmosphere
P91 316L	5°C/min	400°C-3 h	650°C-3 h	1050°C-0.5 h	Ar
Inconel 600 Ni	5°C/min	400°C-3 h	650°C-3 h	1100°C-2 h	Ar

2.3. Corrosion tests in molten chlorides

NaCl and KCl anhydrous salts (> 99 wt.% purity) were purchased from Alfa Aesar, Germany. The salt mixture used for the corrosion experiments was prepared in hermetic plastic containers by weighing the desired amounts of salts according to the eutectic composition (44.5 NaCl-55.5 KCl in wt.%, i.e. 50.6 NaCl-49.4 KCl in at.%). The plastic containers were carefully sealed with a tight moisture-barrier and stored in a desiccator between each use to prevent moisture contamination. Before exposure, the salt mixture was homogenized for 2 h at room temperature using a TURBULA® mixer. Based on the target temperature for third-generation CSP plants, the temperature selected for the corrosion experiments was 700°C [15,34]. As previously shown in Refs. [21,22], all

elements in contact with the salt mixture and the metallic samples (i.e. crucibles, lids and rods, see Fig. 1a) were in alumina to avoid galvanic coupling effects and because of its chemical inertness in molten chlorides [23]. The alumina components were systematically baked in air at 1000°C for 24 h prior to the corrosion experiments following ISO 17245 [42]. The sample dimensions were measured with a digital micrometer (mean of 5 different measurements with a maximum deviation of ± 5 µm). Before embedding in the salt mixture, the samples were ultrasonically cleaned in ethanol and dried a second time.

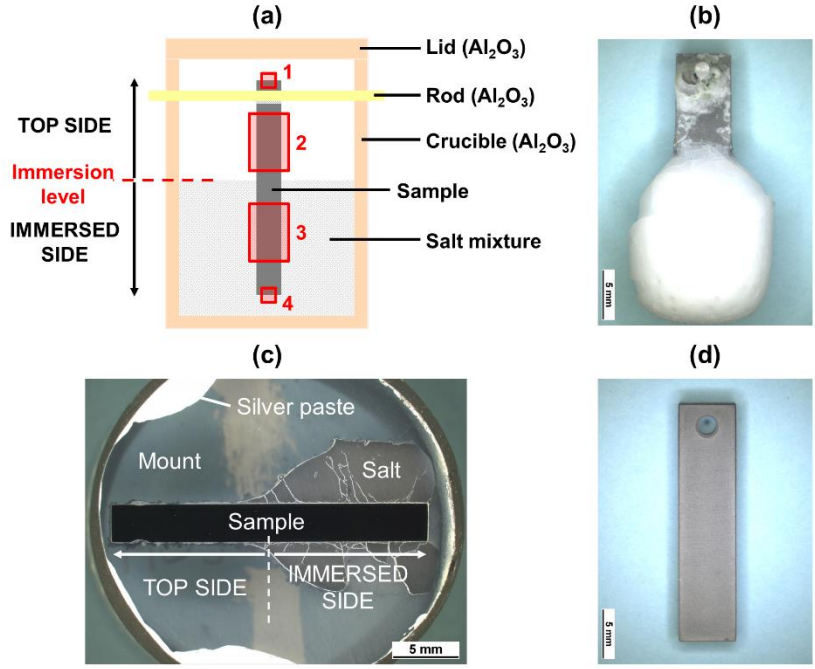

Fig. 1. (a) Schematic representation of the experimental set up used for the molten salt exposure [21], (b) macrograph of an Al-slurry coated 316L sample after partial embedding in molten NaCl-KCl for 100 h at 700°C showing the residual salt mixture attached to the sample and (c) corresponding longitudinal cross-section view of the sample after cold-embedding in epoxy resin and water-free metallographic preparation. For comparison, a macrograph of the Al-slurry coated 316L sample before exposure is given in (d). The locations 1 to 4 correspond to the areas of investigation with, respectively, 1: top edge, 2: outer region, 3: immersed region and 4: bottom edge.

As described in our previous study [21] and depicted in Fig. 1a, the metallic samples were hanged vertically in the alumina crucibles containing approximately 19 g of the eutectic salt mixture (corresponding to a salt content of approximately 8-9 g/cm^2 for the immersed part of the samples). The partial embedding of the samples in the salt mixture allows the investigation of different regions (e.g. initially immersed in the salt or above the salt immersion level) and is particularly informative for screening experiments of different materials. A total of eight samples were placed in the hot zone of a horizontal furnace equipped with a quartz tube. The following procedure is the same used for molten chloride salt exposure of uncoated P91 and Inconel 600 in our previous studies [21,22]. After introduction of the crucibles at room temperature, the furnace was purged with argon (5 ppm water vapor + 2 ppm O_2) at 12 L/h to remove the atmospheric contaminants. The argon flow rate was then decreased to 1.8 L/h before the heating procedure and the absolute pressure of the furnace was maintained slightly above the atmospheric pressure. The furnace was then heated at 5°C/min up to 200°C, held at 200°C for 1 h to remove residual water and further heated at 5°C/min up to 700°C. The temperature was controlled with a Type-S thermocouple and monitored at 700±4°C during the experiment as per ISO 17245 [42]. In this study, the isothermal corrosion test of the Al-slurry coated materials was carried out at 700°C for 100 h under an argon flow of 1.8 L/h. The exhaust gas was treated in a trickle-bed reactor with a NaOH solution to neutralize the acid fumes that may form during the corrosion experiments. At the end of the 100 h isothermal dwell, the samples were left in the furnace to cool down to room temperature.

2.4. Metallographic preparation of the samples

The alumina crucibles were carefully removed from the reaction chamber at room temperature and the samples were systematically taken out of the crucibles paying special attention to preserve salt residues and corrosion products, see Fig. 1b. To prevent absorption of water molecules and allow cross-section preparation, the corroded samples were cold-embedded in epoxy resin by vacuum impregnation (Fig. 1c). The samples were embedded across their longitudinal section to allow the observation of the different locations identified in Fig. 1a corresponding to different testing conditions (i.e. above or below the salt immersion level at the start of the exposure). After curing of the epoxy resin, a water-free metallographic preparation using petroleum oil as lubricant [43] was conducted to prevent the dissolution of water-soluble compounds. Mounted samples were then progressively ground with finer grain down to P2400 SiC paper, polished with 3 µm and 1 µm diamond solutions and cleaned with dry acetone containing molecular sieve. When required, the samples were carbon-sputtered and coated with silver paste to ensure a good electronic conduction (see Fig. 1c). Between each characterization step, the cross-sectioned samples were stored in a desiccator to limit absorption of water molecules and deliquescence of the chlorides. Al-slurry coated materials in the as-manufactured condition were also prepared for microstructural characterization to provide a comparison with corroded samples. These as-coated samples were embedded across their longitudinal section in a conductive resin using a hot mounting press. The cross-section of the samples was then prepared by conventional metallographic methods with a 1 µm polishing finish.

2.5. Microstructural characterization

X-ray diffraction (XRD) was used for the identification of the intermetallic compounds formed on the substrate surfaces after Al-slurry diffusion treatment. The analyses were performed with a BRUKER D8 Advance diffractometer equipped with a LYNXEYE 1D detector in the Bragg-Brentano configuration using Cu $K_{\alpha 1}$ radiation (0.15406 nm). Diffractograms were collected for 2θ angles from 20 to 90° in continuous mode with an increment value of 0.02°. Scanning electron microscopy (SEM) and Energy-dispersive X-ray spectroscopy (EDX) analyses were carried out at 20.0 kV with a HITACHI FlexSEM 1000 II microscope. Electron probe microanalysis (EPMA) was performed with a JEOL JXA-8100 at 15.0 kV to obtain high-resolution elemental maps and concentration profiles (one spot every 1 µm) of the coated samples before and after exposure. A RENISHAW inVia micro-spectrometer equipped with Nd:YAG (λ_{exc} = 532.0 nm) and He-Ne (λ_{exc} = 632.8 nm) laser sources was used for Raman and $Al_2O_3:Cr^{3+}$ fluorescence analyses of the oxides.

3. Results

3.1. Characterization of Al-slurry coated substrates

3.1.1. Ferritic-martensitic P91 steel

Fig. 2a shows the microstructure of Al-slurry coated P91 steel with the identification of three distinct zones (compare with the Al map in Fig. 2b). Zone I is approximately 35 μm thick and contains about 26 at.% Al and 6 at.% Cr (Fig. 2c). To the best of the authors' knowledge, the phase boundary between the disordered A2 and the B2-ordered FeAl has not yet been determined in the Al-Cr-Fe system at temperatures above 1000°C. Nevertheless, Palm noted that there is a complete solid solubility of Cr in A2 and B2 phases at 1000°C [44]. This was recently confirmed by Rank et al. in their detailed experimental investigation of the Al-Cr-Fe system [45]. The latter authors observed that increasing the Cr concentration destabilizes the B2 phase by decreasing the A2/B2 transition temperature and the associated heat effect. For an alloy of nominal composition 25.0Al-5.0Cr-70.0Fe, which is close to the average composition of zone I (Fig. 2c), Rank et al. measured a A2/B2 transition temperature of 741°C and a $D0_3$/B2 transition temperature of 544°C by differential scanning calorimetry (DSC) [45]. For such a composition, the disordered A2 phase is therefore stable at 1050°C whereas the $D0_3$-ordered $Fe_{3-x}Cr_xAl$ phase is the stable compound at room temperature. The XRD diffraction pattern in Fig. 2d indicates the formation of the B2-FeAl as well as $D0_3$-$Fe_{3-x}Cr_xAl$ ordered structures. The identification of the $D0_3$-structure was ascertained with the additional peaks at 2-theta values of about 26.6 and 52.5°, corresponding to the (111) and (311) orientations, respectively [46]. It can therefore be concluded that the disordered A2 phase, stable at 1050°C, underwent a second order transition into the B2-ordered structure and that a fraction of the B2 phase further transformed into $D0_3$-structure upon cooling. These findings are in good agreement with the DSC measurements of Rank et al. in Ref. [45].

Zone II is about 100 μm thick and presents a progressive decrease in Al-content and increase in Cr-content. Small AlN precipitates are observed within this region of the coating as a result of the inward diffusion of Al in the P91 structure and the consequential decreased solubility of N, as commonly observed for aluminization of N-containing steels [27,29,36,37]. In addition, Kirkendall pores developed at the interface between zones I and II (Fig. 2a). These pores most likely result from the imbalance in the diffusion fluxes of Al and Fe in the counter directions during the aluminizing process [27,29]. The C-enrichments observed in the coating layer are associated with the inclusion of the polishing media (see C map in Fig. 2b). Zone III is free of Al (see Al map in Fig. 2b) and corresponds to the P91 steel. The distribution of Mn is homogeneous across the whole thickness of the coating (see Mn map in Fig. 2b) and does not exceed 0.4 at.% in zone I. A similar trend was observed for Mo with an average concentration of 0.3 at.% in zone I.

Since no abrasive treatment was conducted prior to molten salt exposure, it is very likely that a thin alumina scale, which could form during heat treatment and annealing in argon, is still present at the beginning of the immersion in molten chlorides. In fact, the low oxygen partial pressure resulting from the oxygen impurity level of the argon flow (2 ppm in the gas bottle) is still sufficient to oxidize the intermetallic coating as previously reported by Boulesteix et al. in Ref. [47]. The authors conducted Raman-fluorescence analyses and highlighted the formation of a thermally-grown α-Al_2O_3 scale on slurry aluminized P92 steel (annealing at 1050°C for 1 h in their study). The pre-oxidation of the surfaces is expected to play a significant role upon exposure in molten chlorides.

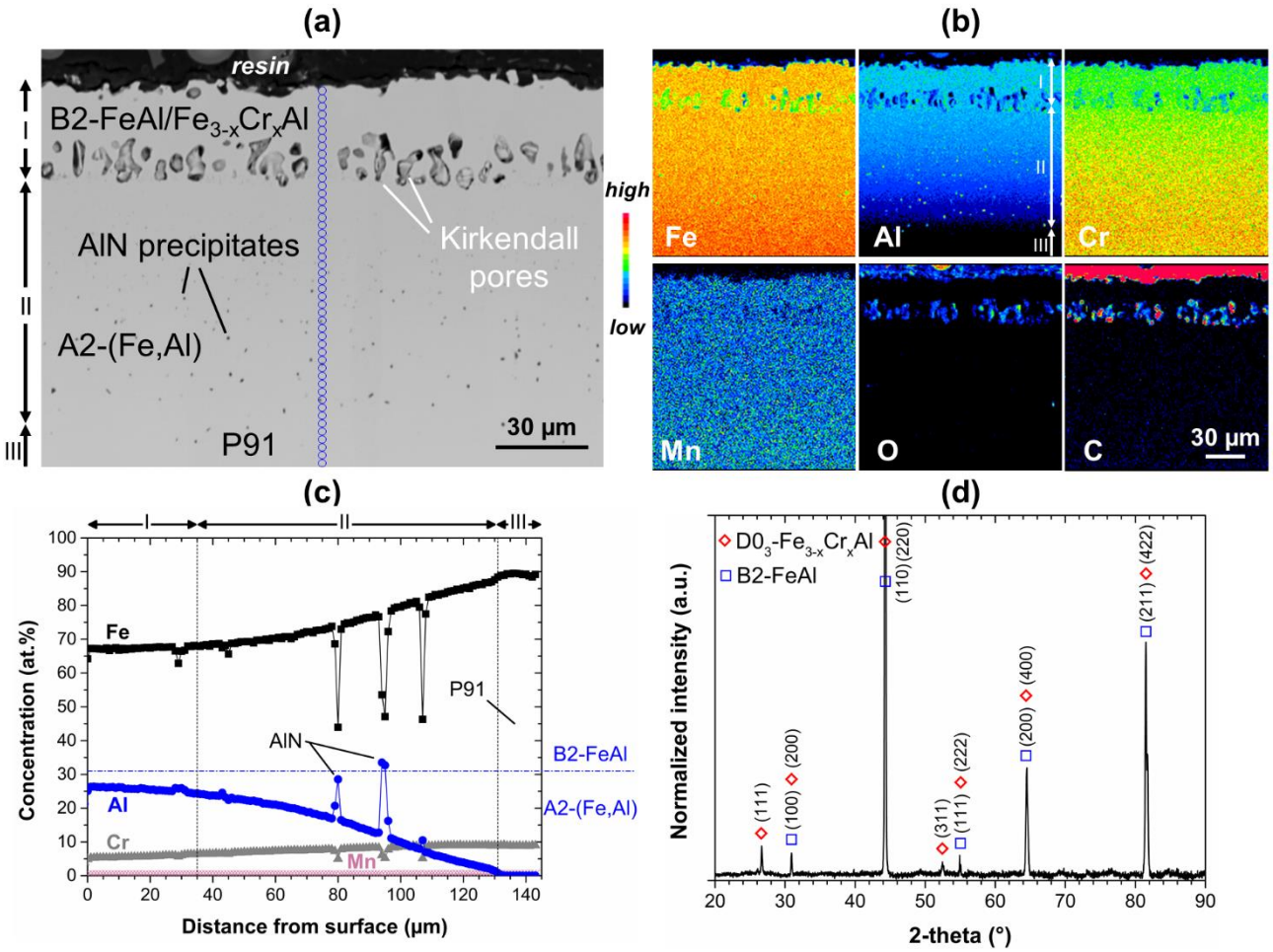

Fig. 2. (a) BSE cross-section image with corresponding (b) EPMA elemental maps and (c) EPMA line scans of Fe, Al, Cr and Mn as well as (d) X-ray diffraction pattern of Al-slurry coated P91 steel. Please note the position of the line scans and zones I to III in (a) and on the Al map (b). The estimated phase boundary between B2 and A2 at the annealing temperature (i.e. 1050°C) from data in Ref. [45] is reported in (c).

3.1.2. Austenitic stainless steel 316L

The cross-section microstructure of Al-slurry coated stainless steel 316L is given in Fig. 3a. The outer region of the coating (zone I) is approximately 40 µm thick with an average composition of 44.0Fe-5.8Ni-39.0Al-9.2Cr-1.1Mn-0.6Mo in at.% corresponding to the B2-(Fe,Ni)Al phase [48]. The formation of a B2-ordered structure was confirmed by XRD with a strong (110) preferential orientation (Fig. 3d). The grain structure of the coating is visible on the BSE cross-section image with an average grain size of 15 µm (average planar diameter). Zone II is characterized by a duplex microstructure with the precipitation of dark spherical particles in a bright matrix (contrast in BSE). According to the EPMA spot measurements, the dark spherical particles are enriched in Al and Ni whereas the matrix is enriched in Fe and Cr (see the line scans Fig. 3c). These observations indicate the precipitation of coherent B2 particles within the Fe-rich A2 matrix since a miscibility gap exists between A2 and B2 phases [48,49]. In addition, dark elongated and blocky precipitates can be observed in zone II and were identified as AlN (N map not shown here). Interestingly, the interfacial region between zones I and II is rich in Ni and comparatively poor in Fe and Cr (see the corresponding maps in Fig. 3b and the line scans in Fig. 3c). Similar features were reported on Al-slurry coated austenitic stainless steel Incoloy 800HT and HR3C [50,51]. However, the relative concentration of the elements in the Ni-rich area is still in agreement with the B2-(Fe,Ni)Al phase by comparison with the ternary Fe-Ni-Al diagram at 1050°C [48]. Zone III is free of Al (compare the Al map in Fig. 3b and the line scan in Fig. 3c) and corresponds to the pristine austenitic structure of stainless steel 316L.

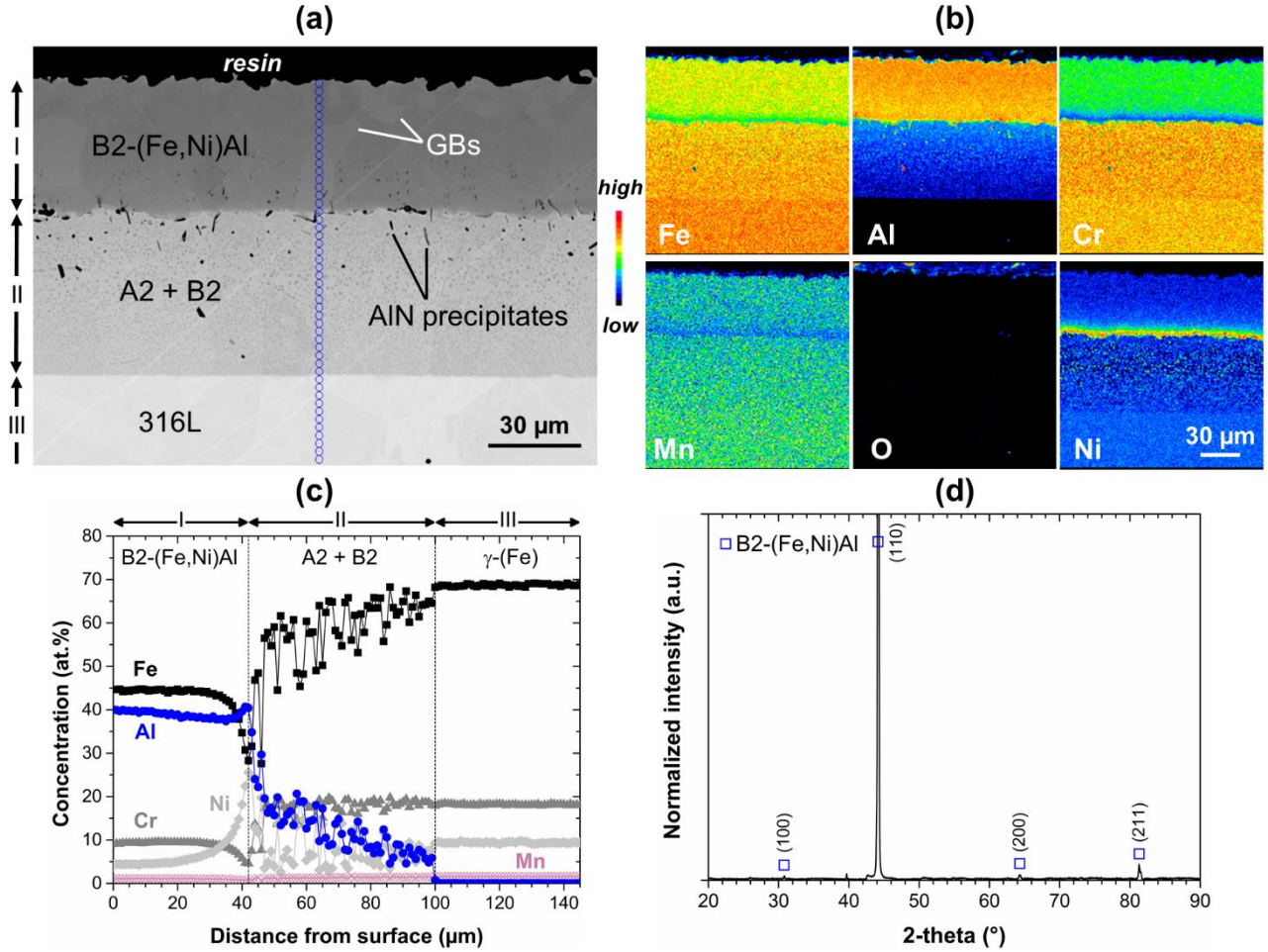

Fig. 3. (a) BSE cross-section image with corresponding (b) EPMA elemental maps and (c) EPMA line scans of Fe, Al, Cr, Ni and Mn as well as (d) X-ray diffraction pattern of Al-slurry coated stainless steel 316L. Please note the position of the line scans and zones I to III in (a).

3.1.3. Inconel 600

Fig. 4a shows the microstructural features of Al-slurry coated Inconel 600. The coating microstructure is typical for high-activity aluminizing [52] with an outer Al-rich β-NiAl layer with Cr-rich precipitates (zone I) and an inner Ni-rich β-NiAl layer almost free of precipitates (zone II). The formation of the intermetallic β-NiAl was confirmed by X-ray diffraction (Fig. 4c). Additional diffraction peaks associated with the precipitation of secondary phases in the Al-rich β-NiAl matrix were identified as Cr_7C_3 and $AlCr_2$ crystal structures. By comparing the BSE cross-section image with the EPMA maps of Ni, Al, Cr and C (Fig. 4b), it appears that the precipitates with an intermediate contrast (in BSE) are Al- and Cr-rich whereas the bright precipitates are C- and Cr-rich. In fact, although approximately 4 at.% of Cr was dissolved in the Al-rich β-NiAl matrix, local Cr-enrichments exceeded 60 at.% of Cr (Fig. 4c). This value of 4 at.% is in good agreement with the reported solubility of Cr in NiAl that is known to decrease with decreasing temperature and increasing Al content [53]. For example, the maximum solid solubility of Cr in stoichiometric NiAl is approximately 8 at.% at 1290°C [53] but only about 4 at.% at 850°C [54]. Complementary EPMA spot measurements were carried out to isolate the composition of the Al/Cr-rich phases and gave an average composition of 63.4Cr-25.6Al-5.7Fe-3.2Ni (main elements in at.%). This composition falls in the α-Cr stability range at 1100°C indicating that the precipitation of α-Cr particles occurred within the coating matrix as a consequence of the limited solubility of Cr in β-NiAl [53]. It is likely that the transformation of these Cr-rich precipitates into $AlCr_2$ (congruent transformation at about 910°C in the Al-Cr binary [55]) occurred upon cooling. The formation of $AlCr_2$ within the aluminide coating is in good agreement with the TEM observations of Chien et al. revealing the precipitation of $AlCr_2$ in α-Cr particles and directly within the β-NiAl matrix for a two-stage aluminized Inconel 600 [56]. In light of the BSE contrast differences, these $AlCr_2$ intermetallic phases are

present as elongated precipitates along the grain boundaries of the Al-rich β-NiAl matrix and fine blocky precipitates inside the grains (Fig. 4a). The chemical composition of the bright precipitates could not be precisely determined due to the limitation of the EPMA spot size, but seems in agreement with the stoichiometry of Cr_7C_3 (Cr concentration in the range 65-70 at.%). The cross-comparison of XRD and EPMA results therefore indicate that the Cr-rich spots visible at the extreme surface of the coating (see map of Cr in Fig. 4b) are associated with the precipitation of fine Cr_7C_3 precipitates as highlighted in the BSE cross-section image. Fine Cr-rich carbides are also distributed in the inner part of zone I and within the Ni-rich β-NiAl layer (see C map in Fig. 4b). Si enrichments up to 3 at.% were detected by EPMA suggesting the precipitation of chromium silicides by comparison of EPMA maps of Cr and Si (not shown). The other alloying elements of Inconel 600 (Mn, Ti) were only detected in small amounts by EPMA (total average composition less than 0.2 at.% in zone I).

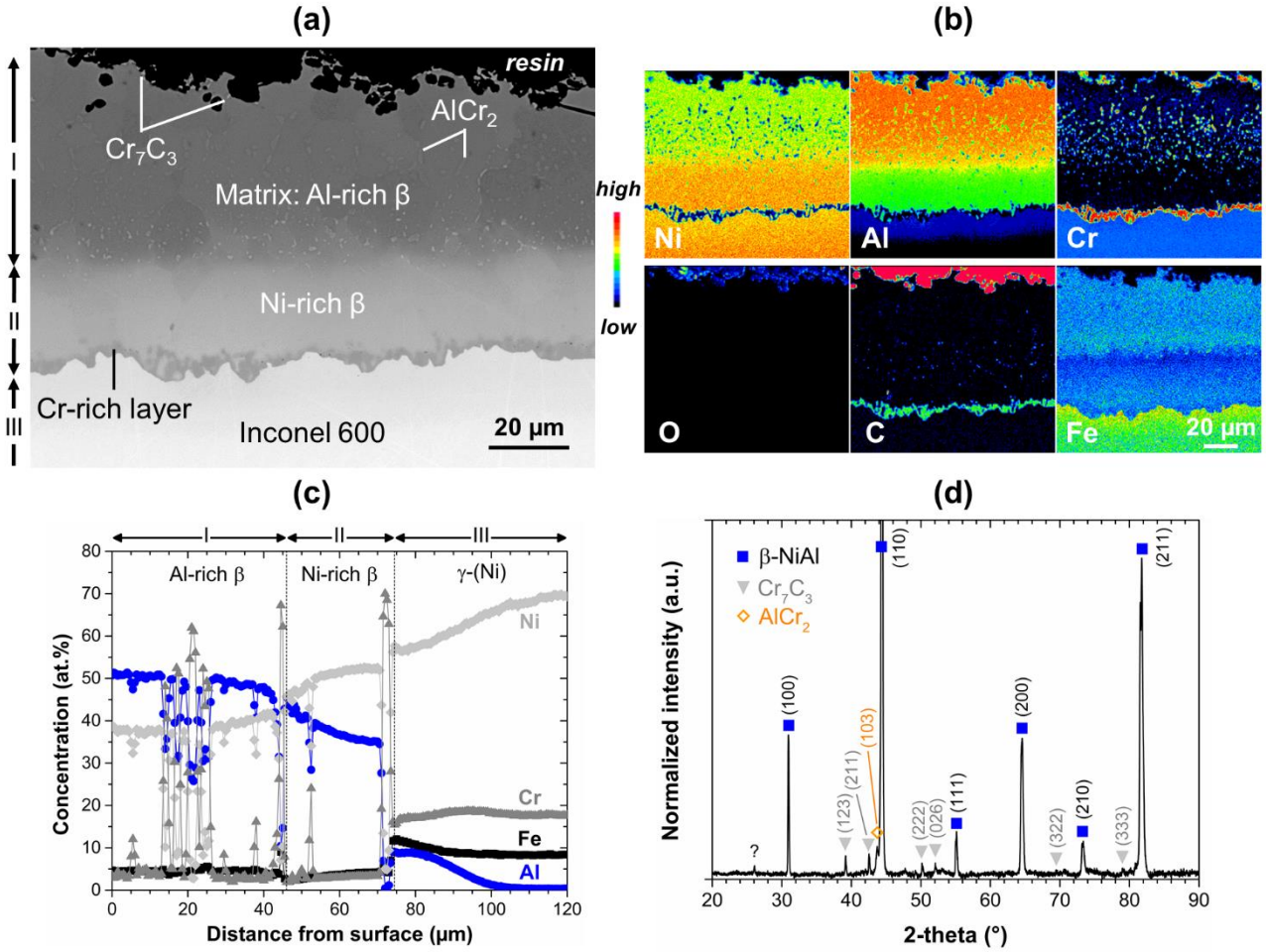

Fig. 4. (a) BSE cross-section image with corresponding (b) EPMA elemental maps and (c) EPMA line scans of Ni, Al, Cr, and Fe as well as (d) X-ray diffraction pattern of Al-slurry coated Inconel 600. Please note the position of the line scans and zones I to III in (a).

At the coating/substrate interface (between zones II and III), a non-planar C- and Cr-rich layer developed. Similar features were reported by Chien et al. for a two-stage aluminized Inconel 600 [56]. These authors indicated that this layer results from the dissolution of a σ phase layer, forming at the aluminizing temperature, into a non-planar $Cr_{23}C_6$-rich layer after annealing at high temperature. The local Cr enrichment was confirmed with the EPMA line scan at about 70 µm from the surface. It is likely that the Cr-rich layer acted as a diffusion barrier for Al inward diffusion upon aluminizing [56,57] resulting in the formation of an Al-rich β-NiAl matrix despite higher annealing temperature and longer annealing time compared to steel substrates. Nevertheless, some Al inward diffusion still occurred below the Cr-rich layer down to about 100 µm from the surface (Fig. 4c), most likely by

solid-state diffusion at the grain boundaries of interfacial Cr-rich phases [56]. The Al concentration does not exceed 9 at.% in this region though, which is lower than the γ-γ/γ' phase boundary at 1100°C [58].

3.1.4. High-purity nickel

Fig. 5a shows the microstructure of Al-slurry coated high-purity nickel with three distinct zones. Zone I is approximately 60 µm thick and is mainly composed of β-NiAl with γ'-Ni_3Al transformation at the grain boundaries. The formation of β-NiAl with the B2-ordered structure was confirmed by X-ray diffraction (Fig. 5d). Kirkendall pores associated with a greater inward flux of Al than outward flux of Ni atoms upon aluminizing are outlined in the outer region of zone I. Twinned structures, associated with the formation of the martensitic β' phase ($L1_0$ structure) can be observed in the inner region of zone I. The diffusionless martensitic transformation of the B2-ordered NiAl compound is well known to occur below a critical Al content upon cooling forming twinned martensite plates in bulk alloys [59,60] and aluminide bond coats [61,62]. The linear dependency of the martensite start temperature (noted M_s) with the composition was first reported by Smialek and Hehemann in Ref. [63]. A best linear fit was given by Noebe et al. with the empirical relation $M_s(K) = 122.8*(at.\%\ Ni) - 7363.6$ [64]. At room temperature (around 25°C), one can therefore expect martensitic transformation of the β-NiAl for a concentration of Al lower than 37.6 at.%. This is in good agreement with the present observations when comparing the composition range of β' (between 36 and 37.6 at.% Al) reported in Fig. 5c and the region of the coating with a twinned microstructure in Fig. 5a. Zone II is approximately 5 µm thick and is poor in Al compared to zone I as highlighted in the Al map (Fig. 5b). According to the stability of Al-Ni phases at 1100°C (see Fig. 5c), zone II

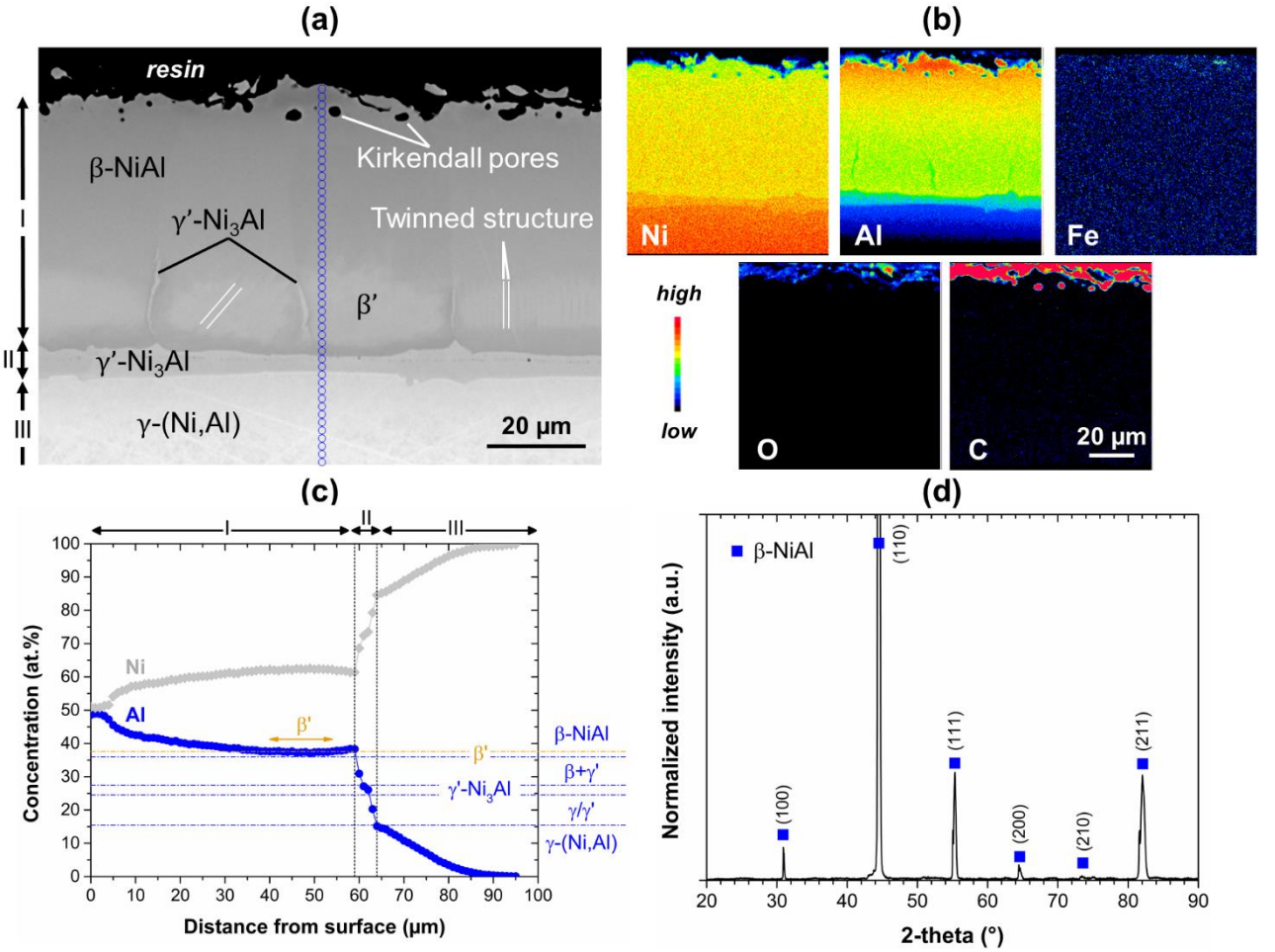

Fig. 5. (a) BSE cross-section image with corresponding (b) EPMA elemental maps and (c) EPMA line scans of Ni and Al as well as (d) X-ray diffraction pattern of Al-slurry coated high-purity nickel. Please note the position of the line scans and zones I to III in (a). The compositional stability of Ni-Al phases at the annealing temperature (i.e. 1100°C) from data in Ref. [46] is reported in (c). The horizontal line at 37.6 at.% Al corresponds to the upper limit to observe martensitic transformation at 25°C according to Noebe et al. [64].

corresponds to the γ'-Ni_3Al phase. Zone III, with a concentration of Al lower than 15.5 at.%, corresponds to a solid solution of Al in Ni and formed as a result of the great concentration gradient between the coating and the nickel substrate. The fact that neither the martensite $L1_0$ nor the γ'-Ni_3Al $L1_2$ structures were detected by XRD may be explained by the limited penetration of the X-rays into the intermetallic coating.

3.2. Corrosion performance of the aluminide coatings

As explained in the experimental section, the Al-slurry coated materials were half-embedded in NaCl-KCl and exposed at 700°C for 100 h in argon atmosphere to evaluate their corrosion performance. The latter was assessed with coating thickness measurements by comparing reference as-coated samples with exposed samples. The results are presented in Fig. 6 in the form of probability plots [65] with as-coated thicknesses and the remaining coating thickness measured after exposure on either the outer region (initially above the melt with easy access of the gas) or immersed region (the readers are referred to Fig. 1a for the corresponding locations). The interpretation of the probability plots is as follows: (1) the *x*-axis corresponds to the probability of a coating thickness not exceeding the corresponding value on the *y*-axis, (2) data fitting a Gaussian distribution appear as a straight line where the slope corresponds to the standard deviation of the data set, (3) a deviation from a straight line can be interpreted as a second distribution such as intergranular attack (termed afterwards as IGA), pitting or scale formation (i.e. passivation). It should be noted that all as-coated samples followed a Gaussian distribution and, apart from Inconel 600, that homogeneous coating layers were produced on the substrates with standard deviation values of up to 6 µm (see the second column in Table 3). However, for most of the testing conditions, two distributions can be identified on the probability plots and were interpreted as areas of the coatings showing a protective behavior or corrosion in the form of IGA, void formation and/or dealloying. The corresponding

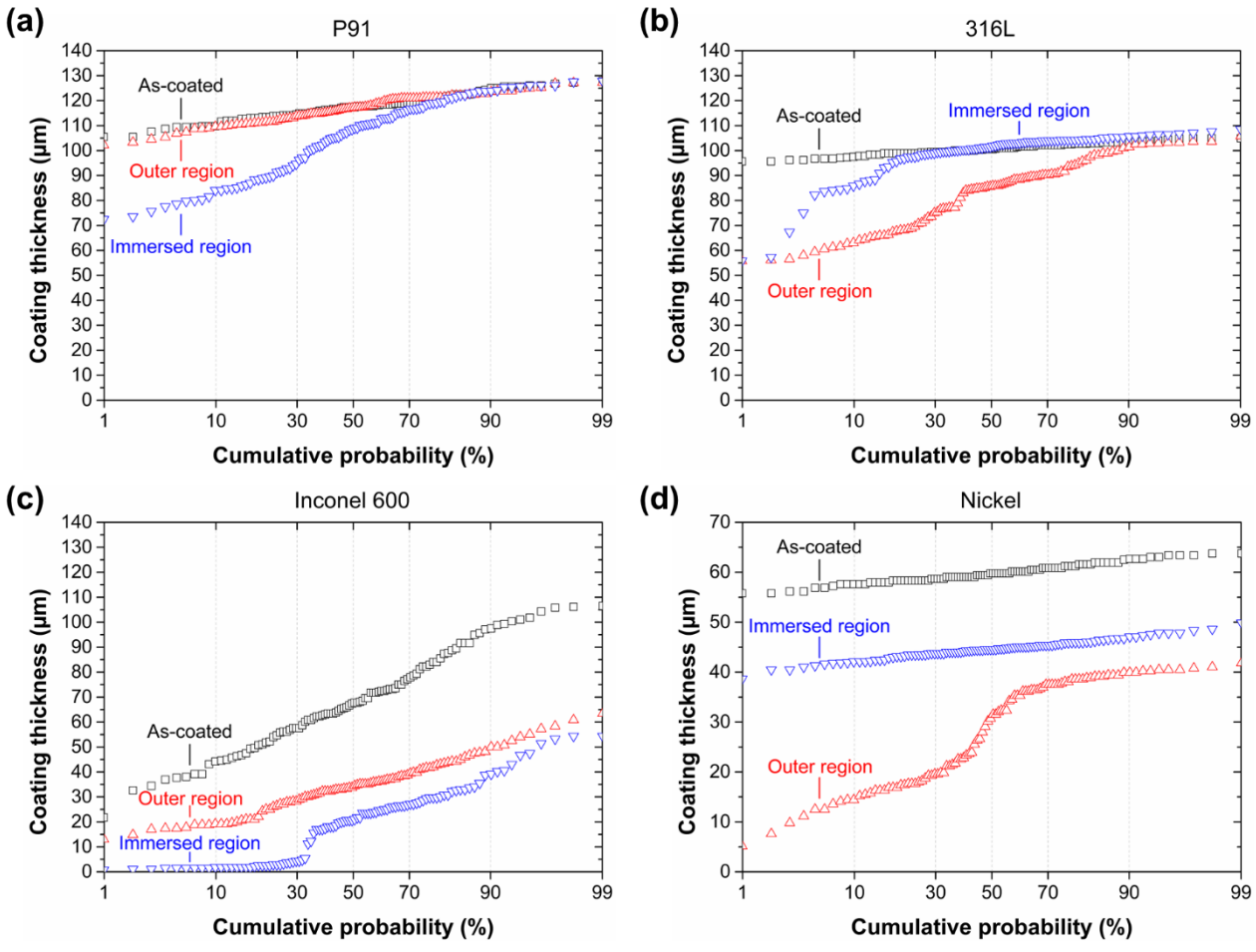

Fig. 6. Summary of coating thickness measurements before (As-coated) and after 100 h exposure to molten NaCl-KCl at 700°C under argon flow in the outer and immersed regions (see Fig. 1a). Probability plots of Al-slurry coated (a) ferritic-martensitic P91 steel, (b) austenitic stainless steel 316L, (c) Inconel 600 and (d) high-purity nickel.

corrosion data extracted from the probability plots on the outer and immersed regions of the samples are summarized in Table 3. For each region and each material, the probability to observe a protective behavior, or alternatively corrosion, is reported. The remaining coating thicknesses with standard deviation values are also given.

Table 3
Summary of the corrosion data extracted from the probability plots for the Al-slurry coated materials. n/a stands for not applicable when the slurry coating was not protective or when no corrosion was observed.

Conditions	As-coated	Outer region				Immersed region			
		Protection		Corrosion		Protection		Corrosion	
Substrate	Coating thickness	Coating thickness	Probability	Coating thickness	Probability	Coating thickness	Probability	Coating thickness	Probability
	(µm)	(µm)	(%)	(µm)	(%)	(µm)	(%)	(µm)	(%)
P91	117±6	117±6	>99	n/a	<1	120±9	≈41	95±18	≈59
316L	101±3	102±6	≈16	79±16	≈84	103±4	≈74	87±26	≈26
Inconel 600	69±20	n/a	<1	34±12	>99	n/a	<1	20±15	>99
Ni	60±2	n/a	<1	28±11	>99	n/a	<1	45±2	>99

From the corrosion data, the following ranking with increasing corrosion performance can be given for Al-slurry coated materials: Inconel 600 < high-purity nickel < austenitic stainless steel 316L < P91 steel. Interestingly, these screening experiments indicate that the order of corrosion resistance is not following the respective concentration of Fe and of Ni of the substrates as commonly reported in the literature when exposing iron- and nickel-based materials to molten chlorides [9,17,18]. In addition, higher concentration in Al does not necessarily improve the corrosion performance of the aluminide coating since Al-slurry coated P91 steel has the lowest Al surface concentration, yet the highest resistance of all coated substrates. These observations suggest that there are several effects on the corrosion performance of the aluminide coatings. This includes the precipitation of secondary phases within the aluminide coatings (e.g. carbides, Cr-rich intermetallic phases), the difference in coefficients of thermal expansion between the aluminide coatings and the underlying substrates, the diffusion fluxes of the elements within the coatings and the occurrence of phase transformation related to Al depletion.

To further compare the corrosion performance of the Al-slurry coated materials, cross-section images taken in various locations of the samples are given in Fig. 7. As observed in Fig. 6b, Al-slurry coated P91 steel was very resistant to corrosion with no apparent degradation on the top edge, outer region and bottom edge (Fig. 7a). Intergranular attack (IGA) of the coating was however observed on the immersed region to a maximum depth of 40 µm. The attack of the coating was associated with the formation of large Al_2O_3 crystals that deposited on the surface (see Fig. 7a, Immersed region). The Al-slurry coated 316L steel (Fig. 7b) shows overall a good corrosion resistance and IGA of the coating was only observed in scarce areas in the immersed region. Nevertheless, the outer region of the samples suffered from IGA with formation of mixed $(Al,Cr)_2O_3$ and $Mn_xCr_{3-x}O_4$ spinel on the surface (identification of the oxide compounds was ascertained by local EDX and Raman spectroscopy analyses as illustrated in Fig. 8). Local attack did not exceed 45 µm and was confined within zone I of the coating. Interestingly, a transgranular crack that formed upon cooling of the sample after the aluminizing process did not show any further sign of attack after exposure (see Fig. 7b, Bottom edge).

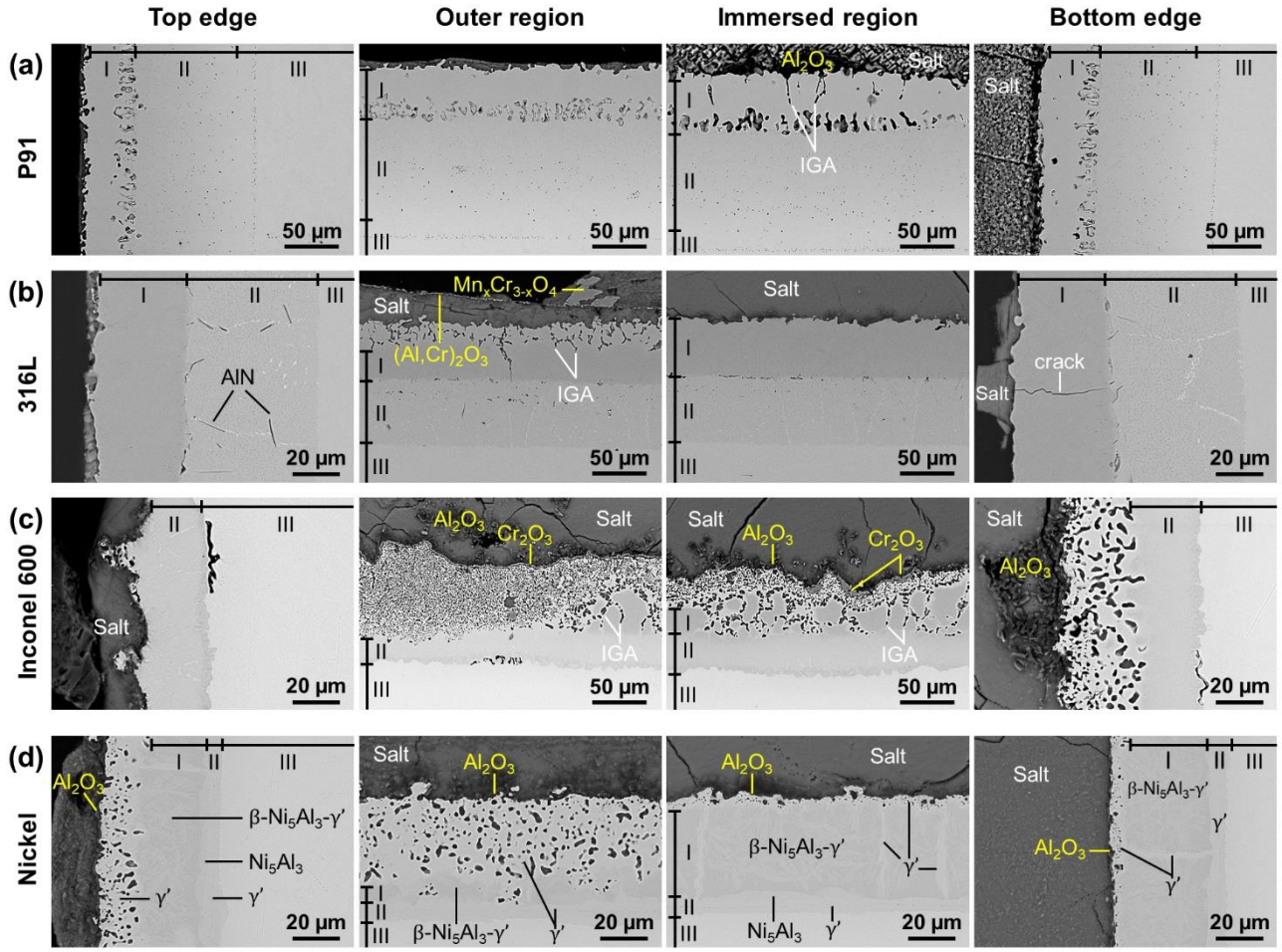

Fig. 7. BSE cross-section images of the Al-slurry coated materials taken in representative locations after 100 h exposure to molten NaCl-KCl at 700°C under argon flow with (a) ferritic-martensitic P91 steel, (b) austenitic stainless steel 316L, (c) Inconel 600 and (d) high-purity nickel. Please note the varying scale bars. The readers are referred to Fig. 1a for the selected locations and to the as-coated substrates in section 3.1 for the identification of zones I-III. IGA: Intergranular attack.

Unlike the two steel substrates, the Al-slurry coating developed on Inconel 600 was not protective in most locations of the sample (Fig. 7c). The aluminide coating was heavily damaged with IGA and subsequent formation of void channels. The Al-rich zone of the coating (i.e. zone I in Fig. 4a) was particularly susceptible to corrosion and was nearly entirely consumed after 100 h of exposure in both outer and immersed regions. The corrosion attack of the coating was associated with the formation of large Al_2O_3 crystals and porous Cr_2O_3 scales that did not protect the coating from further corrosion. However, it is worth mentioning that the coating exhibited superior corrosion resistance in the top edge of the sample. This was ascribed to a lower initial Al concentration with the presence of a Ni-rich β-NiAl layer free of precipitates (compare with Fig. 4a). In all locations, no attack of the Inconel 600 substrate was observed, which indicates the sacrificial role of the aluminide coating in molten NaCl-KCl. Considering Al-slurry coated high-purity nickel, the extent of the corrosion attack was found to be highly dependent on the sample location as illustrated in Fig. 7d. Unlike for the industrial alloys, the corrosion attack of Al-slurry coated high-purity nickel was not associated with IGA but with the progressive formation of void channels (also observed in a later stage of corrosion for Al-slurry coated Inconel 600, see Fig. 7c outer region and bottom edge). Phase transformation occurred within the coating layer with zone I composed of a mixture of β-Ni_5Al_3-γ' phases, typical of Ni-rich β-NiAl compound aged in the vicinity of 700°C as reported by Gheno et al. [66]. As observed for the alloys, Al_2O_3 precipitated as non-protective scales on the surface of the coating.

For a further understanding of the corrosion mechanisms, the next section will present the post-exposure microstructural characterization of coated samples in more details.

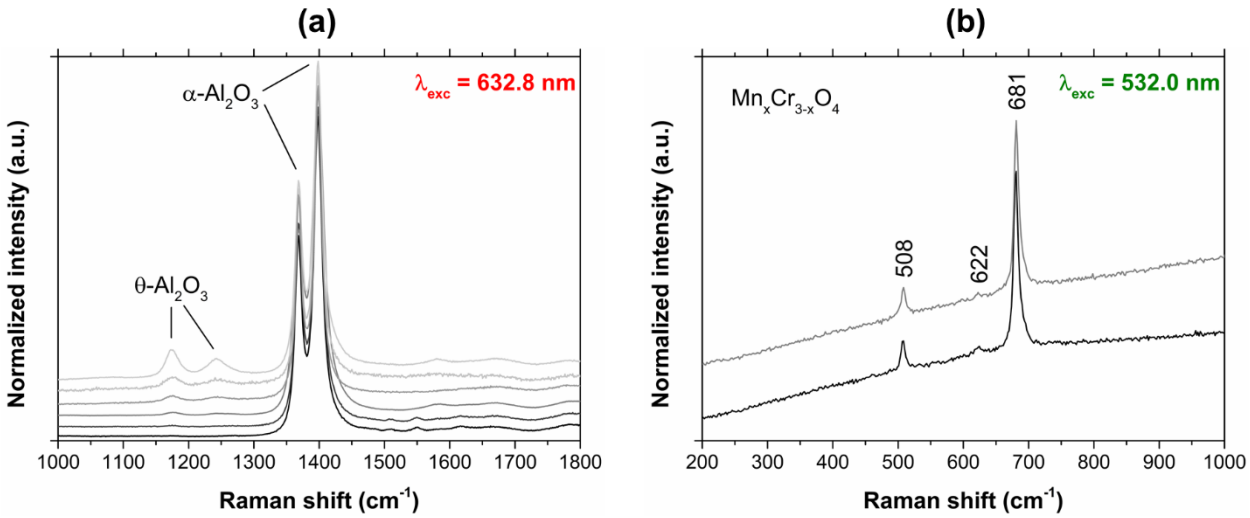

Fig. 8. (a) Identification of θ-Al_2O_3 and α-Al_2O_3 by Cr^{3+} fluorescence and (b) identification of the Raman vibration modes of $Mn_xCr_{3-x}O_4$ spinel for a sample of Al-slurry coated 316L after 100 h exposure to molten NaCl-KCl at 700°C under argon flow. The fluorescence signals given in (a) are representative of all alumina scales observed on the different materials and are systematically composed of α-Al_2O_3 with some θ-Al_2O_3 locally.

3.3. Microstructural characterization of the samples exposed to molten NaCl-KCl at 700°C

3.3.1. Al-slurry coated P91 steel

As deduced from the probability plots in Fig. 6b, the Al-slurry coating offers good protection to P91 steel in molten NaCl-KCl with no apparent degradation on the outer region of the sample (Fig. 9a). In fact, Cl, Na and K maps in Fig. 9b indicate that the salt did not penetrate the aluminide coating. Both Al and Cr concentration profiles are much in line with the ones obtained on the as-coated sample (compare Fig. 9c with Fig. 2c), which indicates that very limited outward diffusion of Al and Cr to form an oxide scale occurred upon exposure. The spot size of the EPMA was too large to ascertain the composition of the oxide scale associated with the O enrichment at the salt/coating interface (Fig. 9b). Because of its high sensitivity, Raman-fluorescence was used instead and confirmed the formation of a thin and protective alumina scale (α-Al_2O_3) as previously reported on Al-coated P91 steel immersed in molten *Solar Salt* [29]. The Kirkendall pores that developed within the coating during the aluminizing process were found to decrease in size with further annealing at 700°C for 100 h (compare Fig. 2a and Fig. 9a). Similar observations were reported by Agüero et al. upon long-term steam exposure of Al-slurry coated P92 steel at 650°C [37].

Despite the overall protective behavior of Al-slurry coated P91 steel, IGA was locally observed in the immersed region (Fig. 9d). As put forward with the Cl, Na and K maps in Fig. 9e, the salt mixture penetrated the intermetallic coating and progressed through the Kirkendall pores by capillary effects. This was confirmed with the EPMA line scan in Fig. 9f showing a Cl enrichment at a distance of 30-50 µm from the salt/coating interface (Na and K line scans were not presented for the sake of clarity but followed the same trend as Cl). In the locations adjacent to IGA, large Al_2O_3 crystals formed on top of the coating (see Al and O maps in Fig. 9e and line scans in Fig. 9f). Apart from local IGA, very limited depletion in both Al and Cr occurred within the intermetallic coating since their mean concentration in zone I is in agreement with as-coated conditions (respectively about 30 and 5 at.%, Fig. 9f).

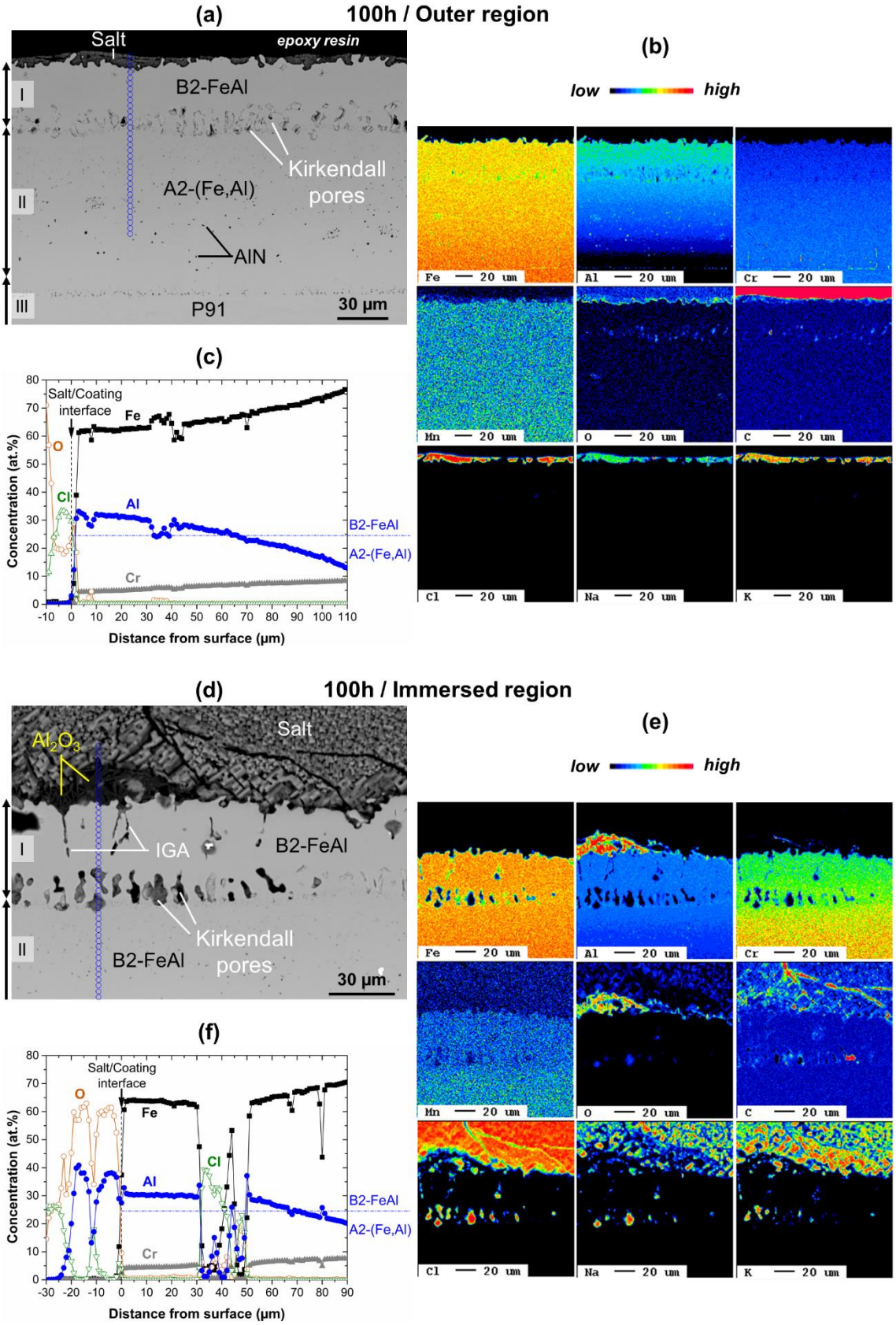

Fig. 9. (a),(d) BSE cross-section images with corresponding (b),(e) EPMA elemental maps and (c),(f) EPMA line scans of Fe, Al, Cr, O and Cl taken in representative areas of Al-slurry coated P91 steel after 100 h exposure to molten NaCl-KCl at 700°C in flowing argon. Please note the position of the line scans in (a) and (d). The phase boundary between B2 and A2 at the testing temperature (i.e. 700°C) from data in Ref. [45] is reported in (c) and (f). Refer to Fig. 1a for the selected locations.

3.3.2. Al-slurry coated 316L stainless steel

Fig. 10a shows the Al-slurry coated 316L stainless steel after exposure to molten NaCl-KCl at 700°C for 100 h in the outer region of the sample. The coating suffered from IGA to a depth of about 20 µm where the penetration of the salt mixture is visible (see maps of Cl, Na and K in Fig. 10b). Whereas the Cr and Ni concentration levels remained constant, the corrosion attack caused a drop of the Al concentration from about 40 at.% to about 35 at.% in the areas adjacent to IGA, see Fig. 10c. This resulted in a comparatively more Fe-rich B2-(Fe,Ni)Al layer. Furthermore, the corrosion attack was associated with the formation of a relatively thin and continuous mixed $(Al,Cr)_2O_3$ scale that detached from the surface of the coating. Large oxide crystals rich in Mn and in Cr are also observed on top of the intermetallic coating (see corresponding elemental maps in Fig. 10b). Raman spectroscopy was carried out to ascertain the composition and structure of the oxides and confirmed the formation of corundum α-Al_2O_3 with local enrichment in θ-Al_2O_3 and of $Mn_xCr_{3-x}O_4$ spinel (with an average stoichiometry of $Mn_{0.87}Cr_{2.13}O_4$ according to local EDX measurements). Al_2O_3:Cr^{3+} fluorescence signals and Raman vibration modes of $Mn_xCr_{3-x}O_4$ spinel are summarized in Fig. 8. Despite the corrosion attack of the coating, it should be noted that in all cases IGA was only observed in zone I of the coating (i.e. within the B2-(Fe,Ni)Al outer layer) and did not proceed further. This feature may be a consequence of the Ni enrichment at the interface between zones I and II of the coating, visible in the Ni map in Fig. 10b, providing better corrosion resistance to the chloride melt than the coating matrix.

Even though Al-slurry coated 316L stainless steel was performant in the immersed region (see Fig. 6c), IGA was locally observed as illustrated in Fig. 10d. The BSE cross-section image was taken in the subsurface region of the coating and highlights the penetration of the salt along the grain boundaries of the coating (see maps of Cl, Na and K in Fig. 10e). As observed for Al-slurry coated P91 steel, Al_2O_3 crystals formed on the surface of the coating in areas adjacent to IGA (compare maps of Al and O in Fig. 10e and the line scans in Fig. 10f). However, the Al concentration profile indicates that limited Al depletion occurred within the coating with a mean concentration of 35 at.%, which still corresponds to the B2-(Fe,Ni)Al stability domain [48]. It is worth mentioning that Mn appeared to be depleted in the subsurface region of the coating as well as in the areas adjacent to IGA (see map of Mn in Fig. 10b and e). This important fact may be associated with the precipitation of secondary phases at the grain boundaries of the coating and their subsequent dissolution. This will be discussed in section 4.2.3. The Si enrichment within the salt was ascribed to the inclusion of the polishing media within the voids where the epoxy resin did not permeate during the vacuum impregnation.

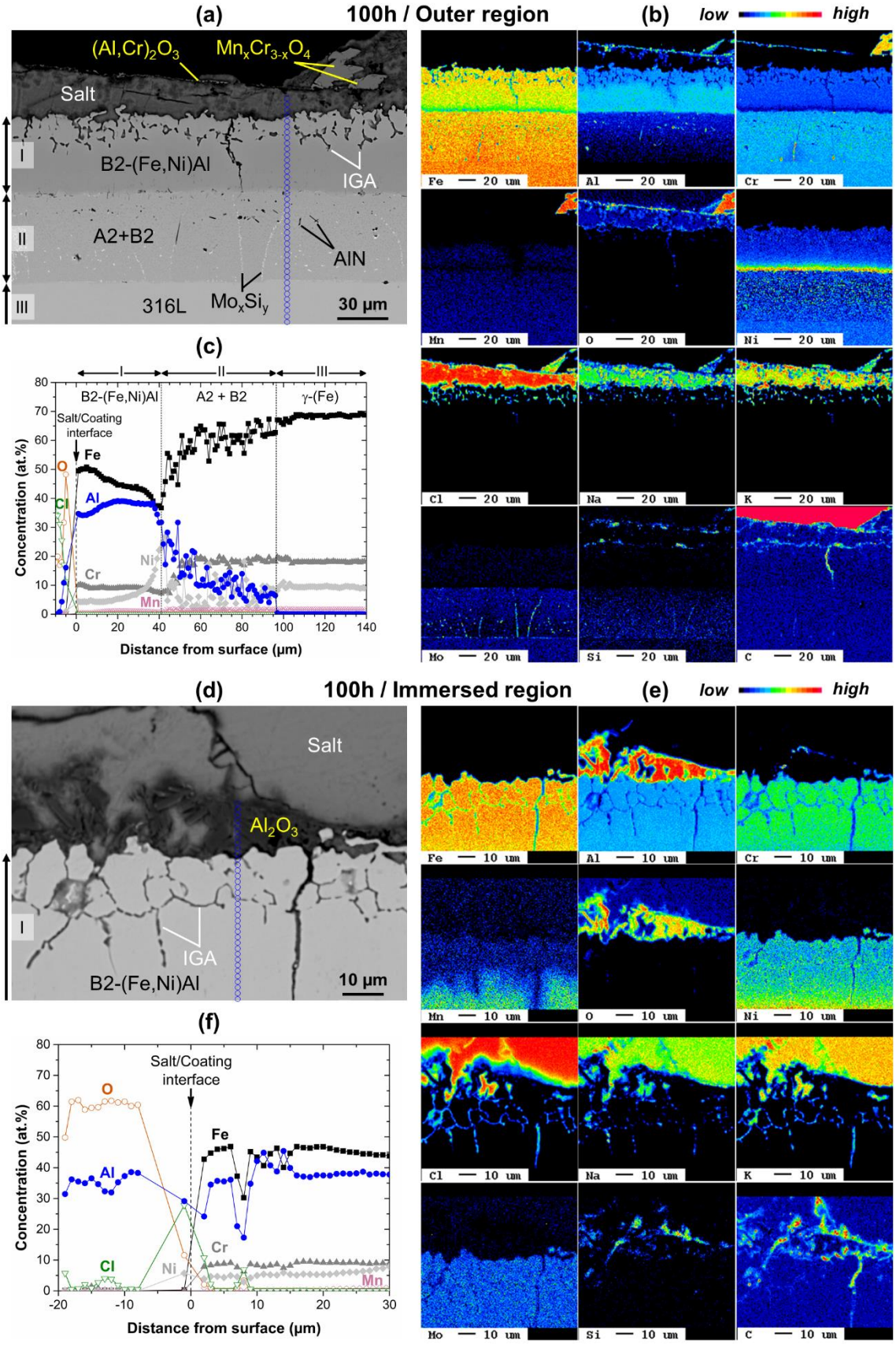

Fig. 10. (a),(d) BSE cross-section images with corresponding (b),(e) EPMA elemental maps and (c),(f) EPMA line scans of Fe, Al, Cr, Ni, Mn, O and Cl taken in representative areas of Al-slurry coated 316L steel after 100 h exposure to molten NaCl-KCl at 700°C in flowing argon. Please note the position of the line scans in (a) and (d). Refer to **Fig. 1**a for the selected locations.

3.3.3. Al-slurry coated Inconel 600

Fig. 11a and c present the cross-section microstructure of Al-slurry coated Inconel 600 after exposure in the immersed region at two stages of the corrosion attack. At an early stage (Fig. 11a), IGA is observed throughout the outer Al-rich β-NiAl layer with penetration of the salt (see maps of Cl, Na and K). Although the EPMA maps of Al and Cr clearly show their depletion from the grain boundaries of the Al-rich β-NiAl matrix, local EPMA spot measurements indicated that such depletion is only revealed within a few microns in the areas adjacent to IGA. The average Al concentration of the Al-rich β-NiAl layer remained constant at approximately 50 at.%, respectively 4 at.% for Cr. The map of Cr shows that the secondary Cr-rich phases that precipitated within the Al-rich β-NiAl grains are still present whereas the ones that precipitated along the grain boundaries are progressively removed, as shown in the magnified view in Fig. 11b. In fact, the formation of void channels along the grain boundaries of the Al-rich β-NiAl layer fairly matches the initial distribution of elongated $AlCr_2$ precipitates (compare with Fig. 4). At this stage, the inner Ni-rich β-NiAl layer is not attacked by the molten salt (Fig. 11a). In addition to IGA, a porous γ'-Ni_3Al layer, appearing brighter than the Al-rich β-NiAl matrix in BSE, started to develop at the coating subsurface region. It is worth mentioning that Cr-rich precipitates are no longer observed in this Al-depleted layer (compare with the map of Cr). The cross-comparison of maps of O, Cr and Al indicates the presence of Cr_2O_3 and Al_2O_3 particles on top of the coating and dispersed within the salt mixture. This suggests that such oxides precipitated as non-protective particles rather than forming continuous and adherent oxide scales on the coating surface. Enrichment in C on top of the coating was attributed to the inclusion of the polishing media.

At a later stage (Fig. 11c), the whole thickness of the coating is damaged resulting in a porous γ'-Ni_3Al layer fully depleted in Cr. The maps of Cl, Na and K highlight the penetration of the salt down to the coating/substrate interface. The magnified view in Fig. 11d shows the porous structure of the intermetallic layer in which the electrolyte progressed by capillary effects. Nevertheless, neither the attack of the substrate nor of the Cr-rich layer was observed, which highlights the sacrificial role of the coating upon exposure. The formation of a thin non-protective $(Al,Cr)_2O_3$ scale and of large Al_2O_3 crystals (visible as dark particles within the salt in Fig. 11c) occurred on top of the corroded coating. In addition, the comparison between BSE cross-section image and Al map suggests the presence of $AlCl_3$ within the NaCl-KCl salt mixture.

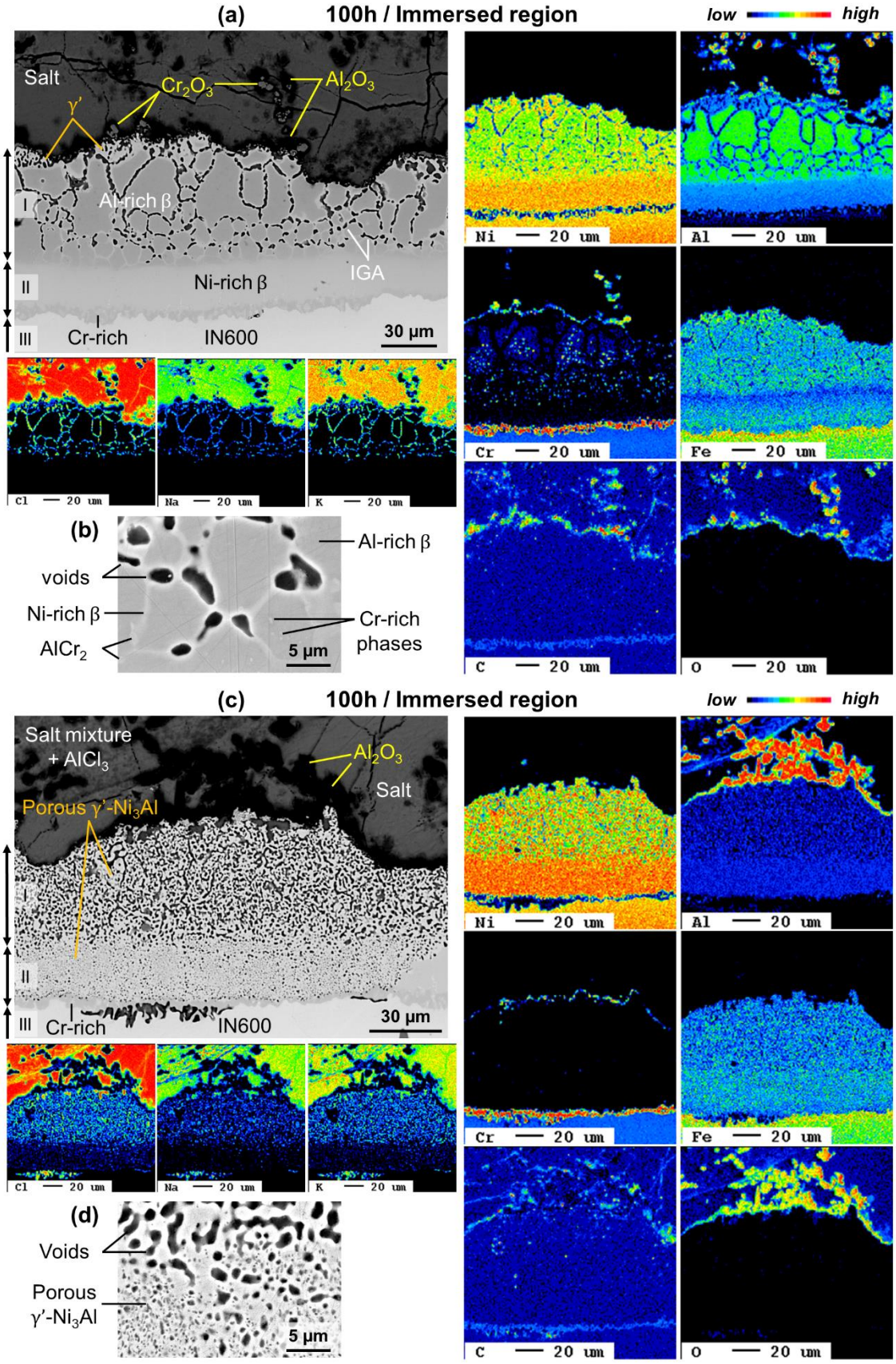

Fig. 11. (a),(c) BSE cross-section images with corresponding EPMA elemental maps taken in representative areas of Al-slurry coated Inconel 600 after 100 h exposure to molten NaCl-KCl at 700°C in flowing argon. Images were taken in the immersed region (Fig. 1a) at two different stages of the corrosion attack. (b) magnified view of (a) at an early stage of the attack showing void formation associated with IGA and Al depletion at the grain boundaries. (d) magnified view of (c) showing the resulting porous γ'-Ni_3Al layer infiltrated with the salt mixture at a later stage of the attack.

3.3.4. Al-slurry coated high-purity nickel

Fig. 12 presents the microstructural characterization of Al-slurry coated high-purity nickel after exposure in molten NaCl-KCl. In the outer region of the sample (Fig. 12a), the aluminide coating is characterized by the development of a porous Al-depleted layer approximately 20 µm thick. With an Al concentration of approximately 25 at.% (Fig. 12b), this layer is composed of γ'-Ni_3Al. As observed with the other materials, the penetration of the salt mixture within the porous region of the coating by capillary effects is highlighted with the maps of Cl, Na and K (Fig. 12b). However, unlike the alloy substrates, the grain boundaries of the coating on high-purity nickel highlighted with the formation of γ'-Ni_3Al do not show accelerated attack. In the inner region of zone I, phase transformation occurred with identification of the Ni_5Al_3 phase presenting an intermediate contrast between γ'-Ni_3Al and β-NiAl phases in BSE. Furthermore, the thickening of the boundary γ'-Ni_3Al layer identified as zone II can be observed by comparison with the as-coated sample in Fig. 5a. This is a consequence of the great Al concentration gradient between the aluminide coating and the nickel substrate that leads to subsequent Al inward diffusion upon exposure at 700°C. The comparison of Al and O maps indicates the formation of a non-continuous Al_2O_3 scale at the coating surface. It should also be noted that a significant amount of Al is dissolved in the salt and most likely indicates the dissolution of Al in the melt forming $AlCl_3$ (compare maps of Al and Cl). The alternating formation of Al_2O_3 and $AlCl_3$ above the salt/coating interface is in good agreement with the varying concentrations of Al, O and Cl in the EPMA line scans presented in Fig. 12c. Interestingly, bright Ni-rich particles are also observed within the salt mixture. Such particles may have detached from the porous γ'-Ni_3Al layer.

As deduced from the coating thickness measurements in Fig. 6e, the corrosion attack was less pronounced in the immersed region of the sample (Fig. 12d) with the formation of a thin porous γ'-Ni_3Al layer in the subsurface of the coating. Unlike the outer region of the sample, very limited dissolution of Al is observed in the salt mixture and only a few Al_2O_3 particles formed on the coating surface. The comparison of the Al concentration profiles of Fig. 12c and f also indicate that limited Al depletion occurred in the immersed region. Nevertheless, the initial β-NiAl coating matrix transformed into a mixture of β-Ni_5Al_3-γ' phases where the γ' phase is usually located at the grain boundaries of the aluminide coating. This transformation occurs in a very narrow concentration range as highlighted with the EPMA line scans, varying between 35 and 40 at.% Al, and is likely to be linked to the initial martensitic transformation of the coating after coating elaboration (Fig. 5). As observed in the outer region, the thickening of the boundary γ'-Ni_3Al layer (i.e. zone II) was noticed after the isothermal exposure at 700°C for 100 h. Despite the occurrence of phase transformation within the aluminide coating, little corrosion was observed in the immersed region indicating that this phenomenon is not the only factor playing a role in the corrosion mechanisms and kinetics.

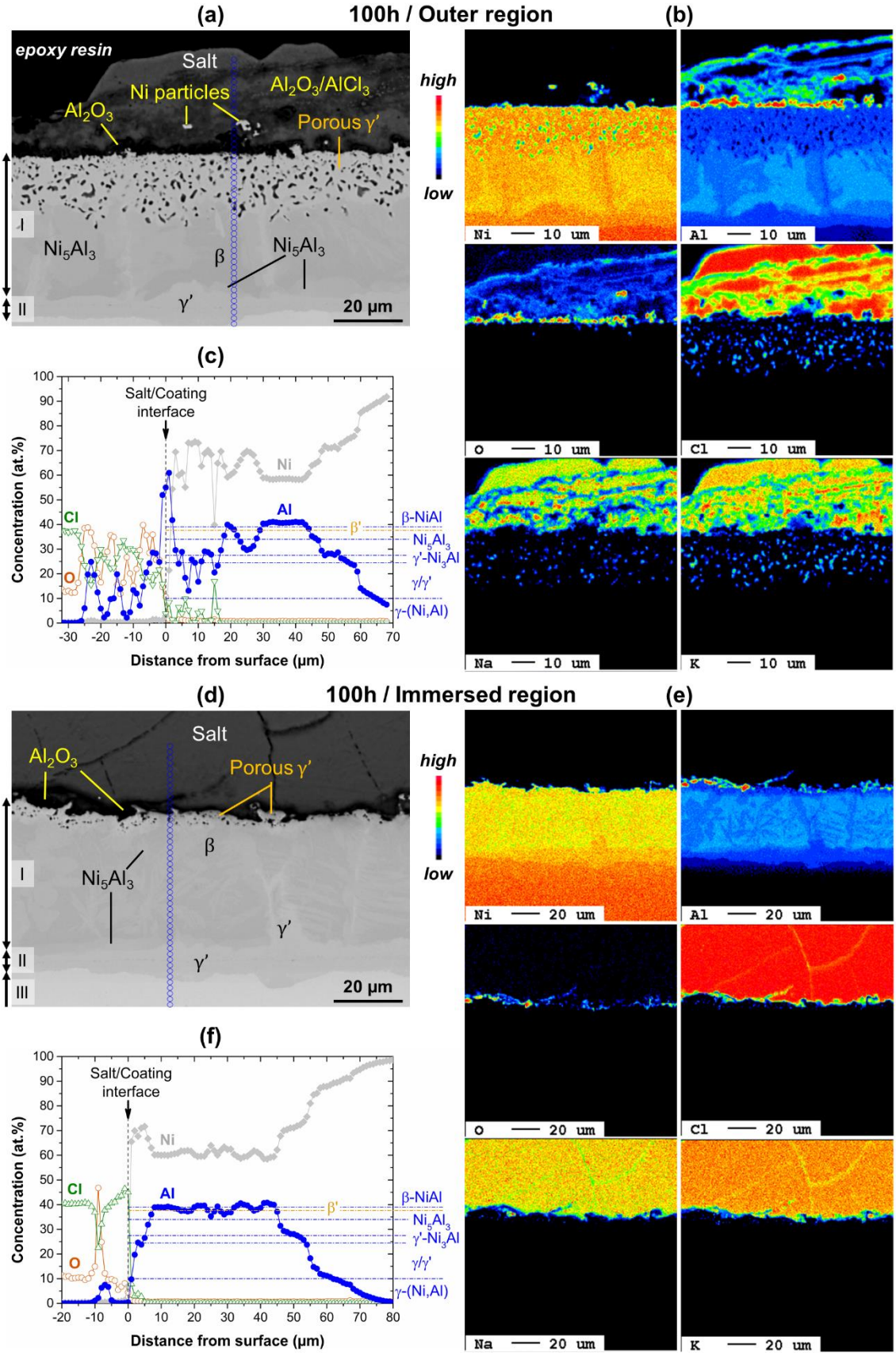

Fig. 12. (a),(d) BSE cross-section images with corresponding (b),(e) EPMA elemental maps and (c),(f) EPMA line scans of Ni, Al, O and Cl taken in representative areas of Al-slurry coated high-purity nickel after 100 h exposure to molten NaCl-KCl at 700°C in flowing argon. Please note the position of the line scans in (a) and (d). The compositional stability of Ni-Al phases at the testing temperature (i.e. 700°C) from data in Ref. [48] is reported in (c) and (f). Refer to Fig. 1a for the selected locations.

4. Discussion

4.1. Slurry aluminizing of the substrates

The mechanisms of formation of slurry aluminide coatings on iron- and nickel-based materials have already been described elsewhere [35,38,67]. It was shown for a slurry containing Al microparticles that the coating layers are formed by self-propagating high-temperature synthesis (SHS) reactions. The reaction process involves (i) emptying of first Al microparticles, wetting and dissolution of the substrate in molten Al, (ii) formation of Al-rich intermetallic compounds (highly exothermic) and self-propagated high-temperature synthesis controlled by Al supply and (iii) solid-state diffusion of Al and of substrate elements once the Al reservoir is consumed. Since the formation of aluminide phases is highly exothermic and local temperatures exceed the melting point of synthesized products, rapid dissolution of iron and nickel substrates occurs in molten Al. This results in the predominant inward diffusion of Al upon aluminizing since the interdiffusion coefficient of Al in Al-rich intermetallic compounds (e.g. Fe_2Al_5, Ni_2Al_3) is significantly larger than that of Fe and/or Ni. Consequently, the coatings produced by this process are of the high-activity type and the annealing at high temperature (i.e. 1050°C for steel substrates and 1100°C for nickel-based substrates) was intended to stabilize B2 aluminide structures [52].

Despite the high-activity of Al upon aluminizing, relatively "clean" aluminide coatings free of secondary precipitates were produced on P91 steel (Fig. 2), 316L stainless steel (Fig. 3) and high-purity nickel (Fig. 5) after the annealing treatment. This was not the case on Inconel 600 with the precipitation of secondary phases within the Al-rich β-NiAl coating matrix (Fig. 4) mainly identified as blocky $AlCr_2$ intermetallics and fine Cr-rich carbides, which is in good agreement with the TEM observations of Chien et al. [56]. It is worth noting that these secondary phases predominantly precipitated at the grain boundaries and triple junctions of the aluminide coating. In addition, the low solubility of C in the austenitic structure of Inconel 600 led to the formation of a Cr-rich boundary layer (essentially as $Cr_{23}C_6$ precipitates after the annealing treatment) at the interface between the substrate and the coating. Such a layer most likely resulted from the decomposition of a non-planar σ layer formed during the aluminizing step at 650°C [56] acting as a diffusion barrier for further Al ingress into the substrate [38,57]. This produced a coating with a higher surface roughness (compare coating thickness measurements for as-coated samples in Fig. 6) and a higher Al surface concentration than the steel substrates and high-purity nickel (compare EPMA line scan measurements).

It can be concluded that the limit of solubility of Cr in aluminide phases and that the C content of the substrate are critical factors governing the mechanisms of formation of slurry aluminide coatings and their resulting microstructure. These microstructural observations are of paramount importance for the corrosion behavior in molten chlorides.

4.2. Factors governing the corrosion performance of iron and nickel aluminides in molten chlorides

4.2.1. Elemental surface activities

Fig. 13a presents the calculated surface activities at 700°C of Cr, Al, Fe and Ni for the Al-slurry coated substrates. For all three alloys, Cr has the highest surface activity of all elements with a maximum value of 0.56 for Al-slurry coated Inconel 600 followed by 316L stainless steel (0.47) and P91 steel (0.36). Similarly, as-coated Inconel 600 has the highest Al surface activity (1.17×10^{-2}) followed by 316L stainless steel (8.7×10^{-3}) and P91 steel (1.6×10^{-3}) whereas its activity is only 2.1×10^{-5} for high-purity nickel. The order of increasing corrosion resistance of aluminide-coated alloys (Inconel 600 < 316L < P91) therefore appears to be inversely correlated to the surface activities of Cr and of Al. These observations are of significant importance since Cr and Al are usually attributed to be highly beneficial for the oxidation and corrosion resistance of alloys at high temperature. On the other hand, the relative surface activities of Fe (maximum for P91) and of Ni (minimum for 316L) appear not to follow the usual order of corrosion resistance attributed to uncoated alloys in molten chlorides, e.g. in Ref. [17]. Such

discrepancies highlight the electrochemical nature of the corrosion attack that is driven by the precipitation of secondary phases within the B2 aluminide matrix of coated alloys rather than its intrinsic Al reservoir nor its relative contents in Fe and in Ni.

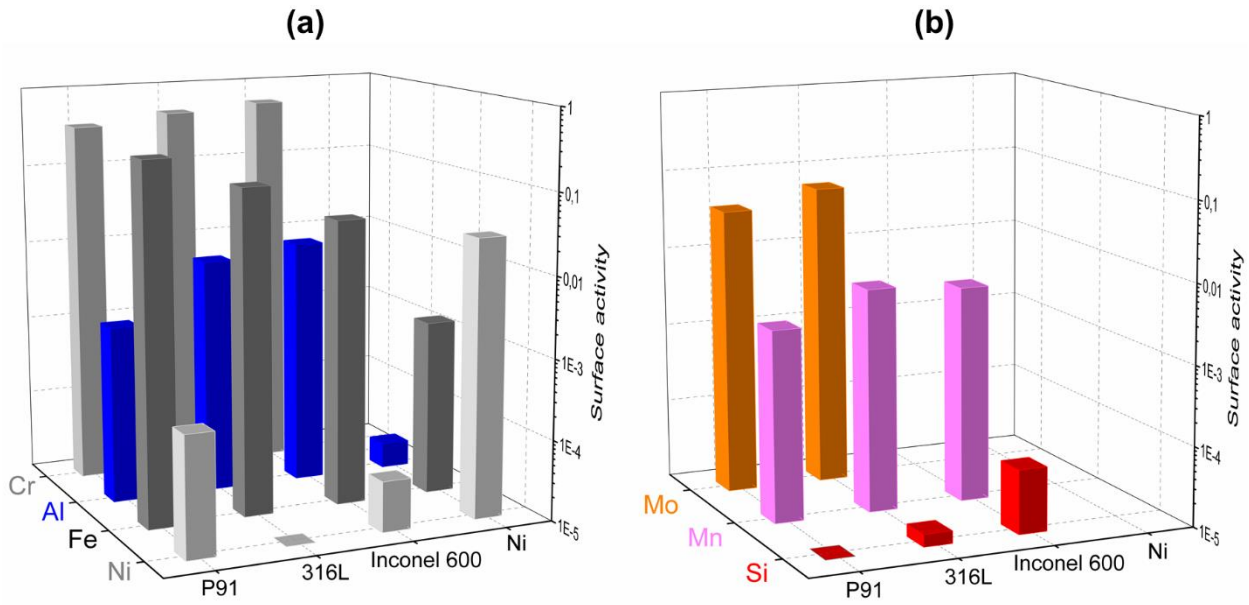

Fig. 13. Calculated surface activities at 700°C of (a) Cr, Al, Fe, Ni and (b) Mo, Mn, Si for the surface composition of Al-slurry coated substrates (JMatPro software).

This is further highlighted when comparing the calculated surface activity of minor elements (Fig. 13b) with that of main elements (Fig. 13a). In fact, whereas the average surface concentration of Mo is only about 0.3 and 0.6 at.% for Al-slurry coated P91 and 316L steels, respectively, its calculated surface activity is actually higher than that of Al by approximately one order of magnitude. Similarly, the calculated surface activity of Mn for the three Al-slurry coated alloys is non-negligible as it appears in the same order of magnitude than that of Al. Finally, the surface activity of Si for both coated steels is relatively low but is non-negligible for coated Inconel 600, most likely due to the limited solubility of Cr in Al-rich β-NiAl and the propensity for the precipitation of chromium silicides in the coating as suggested in section 3.1.3.

From the calculated surface activities of the elements, it can therefore be concluded that the phase distribution of Cr within the coating matrix is the main factor governing the corrosion performance of the aluminide coatings on alloy substrates. As such, the relative Fe and Ni contents of the aluminide coatings have no major influence on their corrosion performance but change the limit of solubility of Cr and the consequential susceptibility for the formation of Cr-rich secondary phases. Since Cr has a complete solubility in B2-FeAl [44] but a low solubility in Al-rich β-NiAl, even in the range of 700°C [54], the precipitation of Cr-rich phases within the coating matrix of Inconel 600 is clearly the life-limiting factor due to their selective dissolution (see Fig. 11a and b). This effect is exacerbated by the considerable activity of Mo on coated steels and its absence on Inconel 600. In fact, Mo is well known to improve the corrosion resistance of alloys in molten chlorides and, from the surface activity calculations of this study and the observations of Sun et al. [16], it can be concluded that Mo effectively prevents the outward diffusion of Cr and blocks active sites for corrosion (i.e. ennobling effect that inhibits anodic dissolution). On the other hand, Mn is expected to decrease the performance of iron and nickel aluminides as a stronger carbide-forming element than Cr as well as its low electrode potential in molten chlorides [25]. The influence of Mn was probably masked by the low solubility of Cr in Al-slurry coated Inconel 600 but was highlighted on coated 316L where its selective dissolution from the coating matrix occurred upon exposure (see Fig. 10b and e). Its combination with Cr and O led to the formation of non-protective Mn-Cr spinel (Fig. 10a). From the Mn maps, it appears likely that Mn-rich

phases segregated at the grain boundaries of the coating and were subsequently dissolved in the melt, implying bulk diffusion of Mn within the coating matrix towards the grain boundaries. In addition, only marginal Cr depletion of the aluminide coating was observed on exposed Al-slurry coated 316L suggesting that Mn-rich phases may have formed instead of Cr-rich phases. This is in good agreement with thermodynamic calculations since Mn is a stronger carbide-forming element than Cr.

These observations, however, do not apply to Al-slurry coated high-purity nickel since the raw material only contains traces (<1 ppm) of Cr and of Mn and is free of Mo, Fe being the largest impurity according to the supplier (≈15 ppm). This indicates that another factor than the precipitation of secondary phases must be responsible for the corrosion attack of Al-slurry coated high-purity nickel. In addition, the selective dissolution of most active elements (e.g. Al, Mn, Cr) upon exposure to molten chlorides will change the surface activity of all elements over time and potentially lead to a change in the corrosion mechanisms and/or kinetics.

4.2.2. Phase transformation and galvanic coupling effects

As discussed in sections 4.1 and 4.2.1, the substrate composition has a direct impact on the microstructure and phase composition of the aluminide coatings. Since all substrates are initially free of Al, a large concentration gradient of Al is established between the coated layers and the substrates at 700°C. This implies that coating degradation by Al inward diffusion into the substrate should be considered as one of the factors influencing the corrosion performance of Al-slurry coated materials in molten salts. Nevertheless, the elemental concentration profiles of exposed samples indicated that such effects were only significant for high-purity nickel after 100 h at 700°C, resulting in the thickening of the intermediate γ'-Ni_3Al layer (i.e. zone II) and the progressive transformation of the β-NiAl coating matrix into a mixed β-Ni_5Al_3-γ' microstructure over time (Fig. 12). Even though no electrochemical data could be found in the literature to question our hypothesis, it is very likely that each aluminide phase has a specific electrode potential in molten chlorides and that Al-rich phases (e.g. β-NiAl, Ni_5Al_3) must have a lower electrode potential than Ni-rich phases (e.g. γ'-Ni_3Al) based on their respective activities in Al (active element) and in Ni (comparatively noble element). The occurrence of phase transformation is therefore expected to generate galvanic coupling effects between the different intermetallic phases in contact with the electrolyte (molten NaCl-KCl). As such, and because of the low oxygen partial pressure in the melt preventing the growth of an insulating alumina layer on intermetallic compounds, β-NiAl (and possibly Ni_5Al_3 too) are selectively dissolved whereas γ'-Ni_3Al is unaffected by corrosion. This hypothesis is in good agreement with the experimental observations since the corrosion attack of Al-slurry coated high-purity nickel leaves a porous γ'-Ni_3Al layer that does not seem to be attacked but that is rather thickening depending on local conditions (compare Fig. 12a and d). This is also consistent with the fact that, unlike coated alloys, the grain boundaries composed of γ'-Ni_3Al are not preferentially attacked for the coated nickel sample. A similar process may be expected for Al-slurry coated Inconel 600 once Cr-rich phases are selectively dissolved leaving a β-NiAl coating matrix free of precipitates that further transforms into a porous γ'-Ni_3Al as illustrated in Fig. 11a and d.

Whereas most studies in the literature indicate that active elements such as Al and Cr are selectively dissolved from the matrix of alloys, our experimental observations suggest that phase dissolution may instead occur such that all elements present in the phase will be dissolved (including Ni). In fact, the galvanic corrosion effects that seem to take place on uncoated [19-22] and aluminide-coated alloys in the present study can be generalized to the contact of any dissimilar phases with a strong electrolyte such as molten NaCl-KCl. This electrochemical process implies that a phase with a lower electrode potential acts as the anode and that a phase with a higher electrode potential acts as the cathode in a similar fashion as the dezincification process of brass alloys or the dealuminification of aluminium bronze alloys. The dissolution of more noble elements such as Ni into Ni^{2+} cations in the melt can in turn feed the cathodic reactions besides oxygen and other oxidants present in the melt. The cathodic reduction of Ni^{2+} into metallic Ni would therefore occur in a cathodic region, namely γ'-Ni_3Al when considering Al-slurry coated high-purity nickel. This electrochemical corrosion process will lead to the progressive transformation of a continuous β-NiAl layer into a porous γ'-Ni_3Al layer, as observed in Fig. 12a and d and to a later

stage of the corrosion attack of Al-slurry coated Inconel 600 (Fig. 11c and d). On the other hand, Al^{3+} cations produced by the anodic reaction are leached away and either combine with O^{2-} anions to precipitate as non-protective Al_2O_3 crystals above the coating surface or remain in the melt and transform into $AlCl_3$ upon cooling since Al_2O_3 has limited solubility in molten NaCl-KCl depending on local pO^{2-} [68]. In addition, $AlCl_3$ possesses high vapor pressure at 700°C and it is possible that outward transport of Al is further accelerated by $AlCl_3$ gaseous species. The proposed corrosion mechanisms presented in Fig. 14 involves phase transformation within the nickel aluminide coating and the creation of galvanic pairs. Unlike dezincification of brass alloys and dealuminification of aluminium bronze alloys in aqueous solutions, bulk diffusion of selectively leached elements is an important part of the corrosion mechanisms since solid-state diffusion mechanisms are activated at 700°C. The initial concentration of the oxidant (e.g. O_2) greatly influences the intensity of the cathodic reaction and may explain the higher corrosion rates on the outer region of Al-slurry coated high-purity nickel than on the immersed region (Fig. 6d and Fig. 7d). A similar corrosion process is expected to occur on Al-slurry coated Inconel 600 once Cr-rich phases are all dissolved (compare Fig. 11b and d). Because O_2 molecules have limited access to the inner region of the attack by diffusion limitations, re-plating of Ni^{2+} cations is expected to occur more rapidly in this region resulting in the formation of microporous channels where the electrolyte progresses by capillary action (see maps of Cl, Na and K in Fig. 11c).

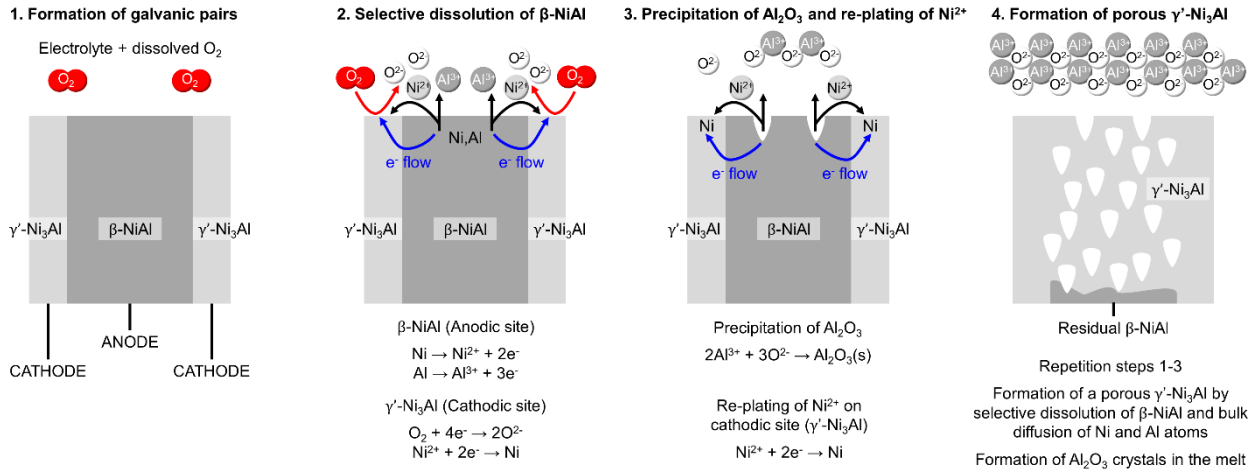

Fig. 14. Schematic illustration of the galvanic corrosion process of β-NiAl resulting in the formation of a porous γ'-Ni_3Al coating layer and non-protective Al_2O_3 crystals above the coating surface. Ni_5Al_3 phase was not considered to simplify the mechanisms but a similar process may be expected between Ni_5Al_3 (anode) and γ'-Ni_3Al (cathode). Unlike dezincification of brass alloys and dealuminification of aluminium bronze alloys in aqueous solutions, solid-state diffusion mechanisms play a major role in the corrosion mechanisms such that phase transformation may trigger the attack.

Likewise, the occurrence of galvanic corrosion effects is a possible explanation for the corrosion attack of coated alloys since Cr_2Al precipitates and Cr-rich carbides appear to be selectively removed from the coating matrix for coated Inconel 600 and since the corrosion attack of coated steels was systematically in the form of IGA. In fact, secondary phases are more likely to precipitate at the grain boundaries and grain triple junctions resulting in the formation of void channels along the grain boundaries after their dissolution as highlighted in the high magnification image in Fig. 11b. The alternating precipitation and dissolution of secondary phases at the grain boundaries thereby leads to IGA and bulk diffusion of selectively leached elements (typically Al, Cr and Mn) from the coating matrix towards the grain boundaries of the aluminide coatings. This hypothesis is particularly documented by the effect of Mn on Al-slurry coated 316L steel considering its relatively high surface activity despite a mean surface concentration of only 1 at.% Mn (Fig. 10a and d). Cr having complete solubility in B2-FeAl [44], the deleterious precipitation of Cr-rich phases occurring on coated Inconel 600 does not occur in coated P91 and 316L steels. This is actually one of the main factors explaining the higher corrosion performance of iron

aluminides than nickel aluminides in molten NaCl-KCl. Another explanation for the superior corrosion resistance of iron aluminides than nickel aluminides is the larger stability domain of B2-FeAl (A2 transformation below 24.5 at.% Al at 700°C [44]) than B2-NiAl (onset of γ' transformation below 39 at.% Al at 700°C [48]). However, both factors clearly indicate that in the absence of phase transformation and/or secondary phase precipitation, a low driving force for corrosion can be expected in molten chlorides under argon. This is in good agreement with the experimental ranking of coated alloys in the order of increasing corrosion resistance: Inconel 600 < High-purity nickel < 316L < P91 and their respective susceptibility to phase transformation and/or secondary phase precipitation.

4.2.3. Influence of testing conditions: oxygen partial pressure and basicity of the melt

As aforementioned, the half-embedding method employed in this study enabled the investigation of different testing conditions on a single sample since half of the sample was immersed in the salt and the other half was above the salt immersion level at the beginning of the exposure (Fig. 1a). Such a design implies a change in the boundary conditions for the outer region of the sample as the melt progressively wets the sample (similar effects were observed in Refs. [21,22]). On the other hand, the lower region of the sample remains in the melt at all times. Therefore, whereas the thin layer of salt that wets the outer region of the sample provides easy access of oxidants (2 ppm oxygen and 5 ppm water vapor according to the impurities contained in the argon flow) from the atmosphere towards the metallic surface, mass transport kinetics will limit the diffusion of oxidants deep in the melt. This design therefore implies the establishment of a concentration gradient of oxidants present in the atmosphere across the longitudinal section of the samples. Since oxygen has a higher solubility in molten chlorides than water [23], it is expected to be the main oxidant in molten chlorides (metallic impurities present in the salts are neglected here but may be an important factor when exposing high-purity active metals, e.g. Cr). The consequential reduction of oxygen into O^{2-} anions will in turn change the local basicity of the melt ($pO^{2-} = -\log a_{O^{2-}}$) such that usual protective scales such as Al_2O_3 may lose their protective behavior and precipitate as non-protective scales above the surface. In addition, microstructural heterogeneities in the aluminide coatings, typically present at the grain boundaries, may lead to *synergistic dissolution* of oxides [69] such that relatively acidic oxides such as Al_2O_3 and Cr_2O_3 are prone to basic fluxing and more basic oxides such as MnO are prone to acidic fluxing following:

$$Al_2O_3(s) + O^{2-} \rightarrow 2AlO_2^- \quad \text{(basic fluxing)} \quad (1)$$

$$Cr_2O_3(s) + O^{2-} \rightarrow 2CrO_2^- \quad \text{(basic fluxing)} \quad (2)$$

$$MnO(s) \rightarrow Mn^{2+} + O^{2-} \quad \text{(acidic fluxing)} \quad (3)$$

These reactions preclude the formation of protective oxide scales at the interface electrolyte/coating such that the electrolyte remains in contact with the metallic phases and that further dissolution of anodic sites occurs. Depending on the local pO^{2-} value, re-precipitation of the oxides may occur as non-protective particles in the melt either as Al_2O_3, Cr_2O_3, $(Al,Cr)_2O_3$ or $Mn_xCr_{3-x}O_4$ as observed in Fig. 7 and confirmed with the high-resolution EPMA maps in section 3.3. In the absence of microstructural heterogeneities and/or dissimilar phases and for an appropriate basicity of the melt, the formation of a thin and dense Al_2O_3 scale is expected to passivate the aluminide coatings and provide protection in molten chlorides. This is in good agreement with the superior corrosion resistance of Al-slurry coated P91 steel and 316L stainless steels and the detection of α-Al_2O_3 by Raman-Cr^{3+} fluorescence analyses on areas unaffected by corrosion. The alumina scale thickness could not be measured with precision due to the proximity of the salt in the embedded cross-sections, but was presumably only a few tenths of a nanometer thick. In such circumstances, the intensity of the electrochemical reactions is very low and no IGA is observed.

Besides electrochemical factors, it is also possible that active oxidation occurs, in which case transport of volatile metal chlorides and their reaction with molecular oxygen above the coating form their corresponding oxide and releases chlorine. The general mechanism can be described by the following steps:

$M(s) \rightarrow M^{n+} + ne^-$	(anodic reaction)	(4)
$M^{n+} + xCl^- \rightarrow MCl_x(g)$	(evaporation of metal chloride)	(5)
$yMCl_x(g) + z/2O_2(g) \rightleftarrows M_yO_z(s) + y.x/2Cl_2(g)$	(active oxidation)	(6)

with M corresponding to one of the active elements (e.g. Al, Cr, Mn). The electromigration of Cl^- due to the production of M^{n+} cations may form volatile chloride compounds (e.g. $AlCl_3$, $CrCl_2$, $MnCl_2$) that diffuse from the metal surface towards the melt. Cl_2 can either diffuse out of the melt, because of a great concentration gradient with the atmosphere, or feed the cathodic reaction. The oxygen partial pressure is the critical factor governing the intensity of the active oxidation process by displacing reaction (6) to the right. Consequently, its effect is expected to be dominant on the outer region of the samples as recently shown for uncoated alloys half-embedded in molten NaCl-KCl [21].

Clearly, electrochemical processes and active oxidation seem to both play a role in the degradation mechanisms as recently proposed by Zhang et al. in a mixed chloride-sulphate melt [70] and by our group in molten NaCl-KCl [21]. Their respective influence is very likely to be a consequence of local thermodynamic conditions such that active oxidation mechanisms are dominating in absence of a melt or when a thin layer of salt is present whereas electrochemical processes are likely to be predominant deep in the melt where access of molecular oxidants from the atmosphere (e.g. oxygen, chlorine) is limited by mass-transport and other oxidants (e.g. Ni^{2+}) may be present. These considerations are of the utmost importance for corrosion issues that may be expected in molten salt storage applications since both factors may lead to very high corrosion rates and localized attack of the containment materials. The changing boundary conditions with the variation of the salt immersion level during the night/day cycles of CSP plants may also trigger these mechanisms.

4.3. Comparison with uncoated substrates for P91 steel and Inconel 600

The corrosion behavior of uncoated ferritic-martensitic P91 steel and Inconel 600 nickel-based alloy in molten NaCl-KCl at 700°C has recently been reported by the authors [21]. Both alloys were found to be sensitive to corrosion by selective leaching of Cr from the alloys and pitting corrosion in the case of P91 steel. Despite the occurrence of IGA for Al-slurry coated P91 steel and the selective leaching of Cr and of Al from coated Inconel 600, the slurry aluminide coatings significantly improved the corrosion behavior of both alloys in molten NaCl-KCl at 700°C. The beneficial role of the aluminide coating is particularly striking for ferritic-martensitic P91 steel since the uncoated alloy was prone to pitting corrosion with local corrosion rates exceeding 10 mm/year in similar testing conditions [21]. In addition, no attack of the substrates was observed in all testing conditions underlining the sacrificial role of the coating. In case of a defect in the coating layer, the iron- or nickel-based substrate would therefore be under cathodic protection by the coating. Slurry aluminizing gives new insights into the cost-effective mitigation of corrosion issues that may be expected in the next generation of CSP plants.

5. Conclusions

The corrosion performance of slurry aluminide coatings in molten NaCl-KCl has been studied. Special attention was paid to investigate the factors governing the corrosion mechanisms and give new insights to propose viable solutions to limit the corrosion of structural materials in molten chlorides. The following specific conclusions can be drawn:

(1) The screening experiments indicate in the order of increasing corrosion performance of Al-slurry coated materials: Inconel 600 < High-purity nickel < Austenitic stainless steel 316L < Ferritic-martensitic P91 steel. It therefore appears that iron-rich aluminides offer better protection than nickel-rich aluminides in molten NaCl-KCl. This was mainly attributed to the larger solubility of Cr in iron aluminides than in nickel aluminides, thereby preventing the precipitation of secondary Cr-rich phases within the B2 aluminide matrix and the consequential formation of galvanic pairs when in contact with the molten salt.

(2) The corrosion attack of Al-slurry coated nickel by molten NaCl-KCl indicates that galvanic corrosion plays a major role in the corrosion mechanisms and that phase transformation within the coating layer (e.g. β-NiAl to γ'-Ni_3Al phase transformation) can trigger this attack. It is proposed that, having a higher activity of Al, β-NiAl (anodic site) is selectively dissolved and that the released Ni^{2+} cations are re-plated on γ'-Ni_3Al (cathodic site). On the other hand, the released Al^{3+} cations combine with O^{2-} to precipitate as non-protective Al_2O_3 particles above the coating surface. This results in the selective leaching of Al from the aluminide coating and the formation of a porous γ'-Ni_3Al layer. These mechanisms are further accelerated by bulk diffusion of Al and Ni atoms.

(3) The impurities in the argon flow (typically oxygen) have an active role in the corrosion kinetics despite relatively low concentrations. This work also highlighted that dissolved metals can effectively act as oxidants (i.e. metal depolarizers) and that further attention must be paid to quantify trace amounts of metals in salt mixtures. This is an important concern for molten salt storage applications as changing boundary conditions during day/night cycles might trigger different corrosion mechanisms and lead to localized damages.

(4) For all materials, no attack of the substrates was observed when the salt mixture progressed through the coating layer, which highlights the sacrificial role of the coating ensuring a cathodic protection to the substrates.

(5) Slurry aluminizing provides new insights into the cost-effective mitigation of corrosion issues that may be expected in the next generation of CSP plants. However, the mechanical behavior of Al-slurry coated alloys should be evaluated to investigate whether the coatings impair their mechanical strength or not and if they trigger stress-corrosion cracking by combination of IGA and creep before industrialization.

Acknowledgements

The European Union's Horizon 2020 research and innovation program is gratefully acknowledged for funding this research (RAISELIFE, grant agreement No. 686008). The authors would like to acknowledge Dr. Gerald Schmidt for conducting EPMA analyses.

References

[1] K. Vignarooban, X. Xu, A. Arvay, K. Hsu, A.M. Kannan, Heat transfer fluids for concentrating solar power systems – A review, *Appl. Energy 146* (2015) 383-396.

[2] A. Bonk, S. Sau, N. Uranga, M. Hernaiz, T. Bauer, Advanced heat transfer fluids for direct molten salt line-focusing CSP plants, *Prog. Energy Combust. Sci. 67* (2018) 69-87.

[3] A. Boretti, S. Castelletto, S. Al-Zubaidy, Concentrating solar power tower technology: present status and outlook, *Nonlinear Eng. 8* (2019) 10-31.

[4] M. Walczak, F. Pineda, A.G. Fernandez, C. Mata-Torres, R.A. Escobar, Materials corrosion for thermal energy storage systems in concentrated solar power plants, *Renew. Sustain. Energy Rev. 86* (2018) 22-44.

[5] J.I. Burgaleta, S. Arias, D. Ramirez, Gemasolar, the first tower thermosolar commercial plant with molten salt storage, *SolarPACES: 17th International Symposium on Concentrated Solar Power and Chemical Energy Technologies*, Granada, September 2011.

[6] A. Bonk, D. Rückle, S. Kaesche, M. Braun, T. Bauer, Impact of solar salt aging on corrosion of martensitic and austenitic steel for concentrating solar power plants, *Sol. Energy Mater. Sol. Cells 203* (2020) 110162.

[7] M. Sarvghad, S. Delkasar Maher, D. Collard, M. Tassan, G. Will, T.A. Steinberg, Materials compatibility for the next generation of concentrated solar power plants, *Energy Storage Mater. 14* (2018) 179-198.

[8] S. Bell, T. Steinberg, G. Will, Corrosion mechanisms in molten salt thermal energy storage for concentrating solar power, *Renew. Sustain. Energy Rev. 114* (2019) 109238.

[9] W. Ding, A. Bonk, T. Bauer, Corrosion behavior of metallic alloys in molten chloride salts for thermal energy storage in concentrated solar power plants: A review, *Front. Chem. Sci. Eng. 12* (2018) 564-576.

[10] Y. Zhao, N. Klammer, J. Vidal, Purification strategy and effect of impurities on corrosivity of dehydrated carnallite for thermal solar applications, *RSC Adv. 9* (2019) 41664-41671.

[11] J.C. Gomez-Vidal, Corrosion resistance of MCrAlX coatings in a molten chloride for thermal storage in concentrating solar power applications, *npj Mater. Degrad. 1, 7* (2017).

[12] G. Salinas-Solano, J. Porcayo-Calderon, J.G. Gonzalez-Rodriguez, V.M. Salinas-Bravo, J.A. Ascencio-Gutierrez, L. Martinez-Gomez, High temperature corrosion of Inconel 600 in NaCl-KCl molten salts, *Adv. Mater. Sci. Eng. 2014* (2014), 696081, https://doi.org/10.1155/2014/696081.

[13] J.C. Gomez-Vidal, A.G. Fernandez, R. Tirawat, C. Turchi, W. Huddleston, Corrosion resistance of alumina-forming alloys against molten chlorides for energy production. I: Pre-oxidation treatment and isothermal corrosion tests, *Sol. Energy Mater. Sol. Cells 166* (2017) 222-233.

[14] J.C. Gomez-Vidal, A.G. Fernandez, R. Tirawat, C. Turchi, W. Huddleston, Corrosion resistance of alumina-forming alloys against molten chlorides for energy production. II: Electrochemical impedance spectroscopy under thermal cycling conditions, *Sol. Energy Mater. Sol. Cells 166* (2017) 234-245.

[15] H. Sun, J. Wang, Z. Li, P. Zhang, X. Su, Corrosion behavior of 316SS and Ni-based alloys in a ternary NaCl-KCl-$MgCl_2$ molten salt, *Sol. Energy 171* (2018) 320-329.

[16] H. Sun, P. Zhang, J. Wang, Effect of alloying elements on the corrosion behavior of Ni-based alloys in molten NaCl-KCl-$MgCl_2$ salt at different temperatures, *Corrosion Sci. 143* (2018) 187-199.

[17] W. Ding, H. Shi, Y. Xiu, A. Bonk, A. Weisenburger, A. Jianu, T. Bauer, Hot corrosion behavior of commercial alloys in thermal energy storage material of molten $MgCl_2$/KCl/NaCl under inert atmosphere, *Sol. Energy Mater. Sol. Cells 184* (2018) 22-30.

[18] W. Ding, H. Shi, A. Jianu, Y. Xiu, A. Bonk, A. Weisenburger, T. Bauer, Molten chloride salts for next generation concentrated solar power plants: Mitigation strategies against corrosion of structural materials, *Sol. Energy Mater. Sol. Cells 193* (2019) 298-313.

[19] A.V. Abramov, V.V. Karpov, A. Yu Zhilyakov, A.F. Gibadullina, I.B. Polovov, V.A. Volkovich, S.V. Belikov, A.V. Shak, O.I. Rebrin, Corrosion of corrosion-resistant and high-temperature nickel-based alloys in chloroaluminate melts, *ECS Trans. 64* (2014) 217-226.

[20] A.V. Abramov, K.V. Dedov, A.F. Gibadullina, A.Y. Zhilyakov, V.V. Karpov, V.A. Volkovich, I.B. Polovov, Corrosive resistance of nickel Hastelloy G-35 superalloy in various aggressive media, *ECS Trans. 86* (2018) 155-162.

[21] B. Grégoire, C. Oskay, T.M. Meißner, M.C. Galetz, Corrosion mechanisms of ferritic-martensitic P91 steel and Inconel 600 nickel-based alloy in molten chlorides. Part I: NaCl-KCl binary system, *Sol. Energy Mater. Sol. Cells 215* (2020) 110659.

[22] B. Grégoire, C. Oskay, T.M. Meißner, M.C. Galetz, Corrosion mechanisms of ferritic-martensitic P91 steel and Inconel 600 nickel-based alloy in molten chlorides. Part II: NaCl-KCl-$MgCl_2$ ternary system, *Sol. Energy Mater. Sol. Cells 216* (2020) 110675.

[23] I.N. Ozeryanaya, Corrosion of metals by molten salts in heat-treatment processes, UDC 620.193.423, Plenum Publishing Corporation (1985) 184-188.

[24] A. Nishikata, H. Numata, T. Tsuru, Electrochemistry of molten salt corrosion, *Mater. Sci. Eng. A 146* (1991) 15-31.

[25] H.C. Gaur, H.L. Jindal, Standard electrode potentials in molten chlorides, *Electrochem. Acta 13* (1968) 835-842.

[26] J. Bouteillon, J.-C. Poignet, Constantes électrochimiques des sels fondus, Techniques de l'Ingénieur, Réf. K825 V1 (1996).

[27] P. Audigié, V. Encinas-Sánchez, M. Juez-Lorenzo, S. Rodríguez, M. Gutiérrez, F.J. Pérez, A. Agüero, High temperature molten salt corrosion behavior of aluminide and nickel-aluminide coatings for heat storage in concentrated solar power plants, *Surf. Coat. Technol. 349* (2018) 1148-1157.

[28] A. Soleimani Dorcheh, M.C. Galetz, Slurry aluminizing: a solution for molten nitrate salt corrosion in concentrated solar power plants, *Sol. Energy Mater. Sol. Cells 146* (2016) 8-15.

[29] C. Oskay, T.M. Meißner, C. Dobler, B. Grégoire, M.C. Galetz, Scale formation and degradation of diffusion coatings deposited on 9% Cr steel in molten solar salt, *Coatings 9* (2019) 687.

[30] P. Audigié, V. Encinas-Sánchez, S. Rodríguez, F.J. Pérez, A. Agüero, High temperature corrosion beneath carbonate melts of aluminide coatings for CSP application, *Sol. Energy Mater. Sol. Cells 210* (2020) 110514.

[31] X. Montero, M.C. Galetz, M. Schütze, A novel type of environmentally friendly slurry coatings, *JOM 67* (2014) 77-86.

[32] Y.S. Li, M. Spiegel, S. Shimada, Corrosion behaviour of various model alloys with NaCl-KCl coating, *Mater. Chem. Phys. 93* (2005) 217-223.

[33] Y.S. Li, M. Spiegel, Models describing the degradation of FeAl and NiAl alloys induced by $ZnCl_2$-KCl melt at 400-450°C, *Corrosion Sci. 46* (2004) 2009-2023.

[34] G. Mohan, M. Venkataraman, J. Gomez-Vidal, J. Coventry, Thermo-economic analysis of high-temperature sensible thermal storage with different ternary eutectic alkali and alkaline earth metal chlorides, *Sol. Energy 176* (2018) 350-357.

[35] M.C. Galetz, X. Montero, M. Mollard, M. Gunthner, F. Pedraza, M. Schütze, The role of combustion synthesis in the formation of slurry aluminization, *Intermetallics 44* (2014) 8-17.

[36] A. Agüero, R. Muelas, M. Gutiérrez, R. Van Vulpen, S. Osgerby, J.P. Banks, Cyclic oxidation and mechanical behaviour of slurry aluminide coatings for steam turbine components, *Surf. Coat. Technol. 201* (2007) 6253-6260.

[37] A. Agüero, K. Spiradek, S. Höfinger, M. Gutiérrez, R. Muelas, Microstructural evolution of slurry Fe aluminide coatings during high temperature steam oxidation, *Mater. Sci. Forum 595-598* (2008) 251-259.

[38] B. Bouchaud, B. Rannou, F. Pedraza, Slurry aluminizing mechanisms of Ni-based superalloys incorporating an electrosynthesized ceria diffusion barrier, *Mater. Chem. Phys. 143* (2013) 416-424.

[39] W. Yan, W. Wang, Y. Shan, K. Yang, W. Sha, 9-12Cr heat-resistant steels, Springer 2015, ISBN 978-3-319-14839-7.

[40] ASM Handbook Volume 4: Heat treating, ASM International 1991, ISBN 087170-379-3.

[41] M.J. Donachie, S.J. Donachie, Superalloys: a technical guide, ASM International 2002, ISBN 0-87170-749-7.

[42] International Standard ISO, Corrosion of Metals and Alloys – Test Method for High Temperature Corrosion Testing of Metallic Materials by Immersing in Molten Salt or Other Liquids Under Static Conditions,17245 (2015).

[43] K. Rahts, M. Schorr, C. Schwaln, M. Schütze, Water-free methods of preparation for the analyses of chlorides in the high temperature oxidation in chloride containing atmospheres, *Prakt. Metallogr. 36* (1999) 86-97.

[44] M. Palm, Concepts derived from phase diagram studies for the strengthening of Fe-Al based alloys, *Intermetallics 13* (2005) 1286-1295.

[45] M. Rank, P. Franke, J. Hoffmann, H.J. Seifert, Experimental investigation of phase equilibria in the Al-Cr-Fe system, *Calphad 66* (2019) 101638.

[46] X. Yan, A. Grytsiv, P. Rogl, V. Pomjakushin, M. Palm, The Heusler phase $Ti_{25}(Fe_{50-x}Ni_x)Al_{25}$ ($0 \leq x \leq 50$); structure and constitution, *J. Phase Equilib. Diff. 29* (2008) 500-508.

[47] C. Boulesteix, V. Kolarik, F. Pedraza, Steam oxidation of aluminide coatings under high pressure and for long exposures, *Corrosion Sci. 144* (2018) 328-338.

[48] L. Eleno, K. Frisk, A. Schneider, Assessment of the Fe-Ni-Al system, *Intermetallics 14* (2006) 1276-1290.

[49] C. Stallybrass, G. Sauthoff, Ferritic Fe-Al-Ni-Cr alloys with coherent precipitates for high-temperature applications, *Mater. Sci. Eng. A 387-389* (2004) 985-990.

[50] C. Boulesteix, B. Grégoire, F. Pedraza, Oxidation performance of repaired aluminide coatings on austenitic steel substrates, *Surf. Coat. Technol. 326* (2017) 224-237.

[51] C. Boulesteix, F. Pedraza, Characterisation of aluminium diffusion coatings elaborated on austenitic stainless steels and on ferritic-martensitic steels, *Surf. Coat. Technol. 339* (2018) 27-36.

[52] G.W. Goward, D.H. Boone, Mechanisms of formation of diffusion aluminide coatings on nickel-based superalloys, *Oxidation Met. 3* (1971) 475-495.

[53] W.H. Tian, C.S. Han, M. Nemoto, Precipitation of α-Cr in B2-ordered NiAl, *Intermetallics 7* (1999) 59-67.

[54] W.F. Gale, J.E. King, Precipitation of chromium containing phases in aluminide coated nickel-base superalloy single crystals, *J. Mater. Sci. 28* (1993) 4347-4354.

[55] Y. Liang, C. Guo, C. Li, Z. Du, Thermodynamic modeling of the Al-Cr system, *J. Alloys Compd. 460* (2008) 314-319.

[56] A. Chien, D. Gan, P. Shen, Microstructures of two-stage aluminized coatings on Inconel 600, *Mater. Sci. Eng. A 206* (1996) 215-224.

[57] M.C. Galetz, C. Oskay, S. Madloch, Microstructural degradation and interdiffusion behavior of NiAl and Ge-modified NiAl coatings deposited on Alloy 602 CA, *Surf. Coat. Technol. 364* (2019) 211-217.

[58] W. Huang, Y.A. Chang, Thermodynamic properties of the Ni-Al-Cr system, *Intermetallics 7* (1999) 863-874.

[59] D. Schryvers, P. Boullay, P.L. Potapov, R.V. Kohn, J.M. Ball, Microstructures and interfaces in Ni-Al martensite: comparing HRTEM observations with continuum theories, *Int. J. Solids Struct. 39* (2002) 3543-3554.

[60] R. Kainuma, H. Ohtani, K. Ishida, Effect of alloying elements on martensitic transformation in the binary NiAl(β) phase alloys, *Metall. Mater. Trans. A 27* (1996) 2445-2453.

[61] Y. Zhang, J.A. Haynes, B.A. Pint, I.G. Wright, W.Y. Lee, Martensitic transformation in CVD NiAl and (Ni,Pt)Al bond coatings, *Surf. Coat. Technol. 163-164* (2003) 19-24.

[62] M. Brossard, F. Pedraza, M. Craig, J.R. Nicholls, Failure mechanism of an out-of-pack nickel aluminide coating cyclically oxidised at 1100°C with water accelerated cooling, *Surf. Coat. Technol. 276* (2015) 649-657.

[63] J.L. Smialek, R.F. Hehemann, Transformation temperatures of martensite in β-phase nickel aluminide, *Metall. Mater. Trans. A 4* (1973) 1571-1575.

[64] R.D. Noebe, A. Misra, R. Gibala, Plastic flow and fracture of B2 NiAl-based intermetallic alloys containing a ductile second phase, *ISIJ Int. 31* (1991) 1172-1185.

[65] International Standard ISO, Corrosion of Metals and Alloys – Method for Metallographic Examination of Samples After Exposure to High-temperature Corrosive Environments, 26146 (2012).

[66] T. Gheno, M. Zahiri Azar, A.H. Heuer, B. Gleeson, Reaction morphologies developed by nickel aluminides in type II hot corrosion conditions: The effect of chromium, *Corrosion Sci. 101* (2015) 32-46.

[67] T. Kepa, F. Pedraza, F. Rouillard, Intermetallic formation of Al-Fe and Al-Ni phases by ultrafast slurry aluminization (flash aluminizing), *Surf. Coat. Technol. 397* (2020) 126011.

[68] T. Ishitsuka, K. Nose, Stability of protective oxide films in waste incineration environment – solubility measurement of oxides in molten chlorides, *Corrosion Sci. 44* (2002) 247-263.

[69] R.A. Rapp, Y.S. Zhang, Hot corrosion of materials: fundamental studies, *JOM 46* (1994) 47-55.

[70] S. Zhang, H. Li, Z. Jiang, B. Zhang, Z. Li, J. Wu, H. Feng, H. Zhu, F. Duan, Chloride- and sulphate-induce hot corrosion mechanism of super austenitic stainless steel S13254 under dry gas environment, *Corrosion Sci. 163* (2020) 108295.